ARTICLE

Collective cancer invasion forms an integrin-dependent radioresistant niche

Anna Haeger[1]*, Stephanie Alexander[2,3,4]* [ID], Manon Vullings[1], Fabian M.P. Kaiser[3], Cornelia Veelken[1], Uta Flucke[5], Gudrun E. Koehl[6], Markus Hirschberg[2,3], Michael Flentje[7], Robert M. Hoffman[8,9], Edward K. Geissler[6], Stephan Kissler[3] [ID], and Peter Friedl[1,2,3,4] [ID]

Cancer fatalities result from metastatic dissemination and therapy resistance, both processes that depend on signals from the tumor microenvironment. To identify how invasion and resistance programs cooperate, we used intravital microscopy of orthotopic sarcoma and melanoma xenografts. We demonstrate that these tumors invade collectively and that, specifically, cells within the invasion zone acquire increased resistance to radiotherapy, rapidly normalize DNA damage, and preferentially survive. Using a candidate-based approach to identify effectors of invasion-associated resistance, we targeted β1 and αVβ3/β5 integrins, essential extracellular matrix receptors in mesenchymal tumors, which mediate cancer progression and resistance. Combining radiotherapy with β1 or αV integrin monotargeting in invading tumors led to relapse and metastasis in 40–60% of the cohort, in line with recently failed clinical trials individually targeting integrins. However, when combined, anti-β1/αV integrin dual targeting achieved relapse-free radiosensitization and prevented metastatic escape. Collectively, invading cancer cells thus withstand radiotherapy and DNA damage by β1/αVβ3/β5 integrin cross-talk, but efficient radiosensitization can be achieved by multiple integrin targeting.

Introduction

Metastatic progression of cancer is initiated by neoplastic cells leaving the primary tumor to migrate into the tumor-free microenvironment (Nieto et al., 2016). Invading cancer cells receive tumor stroma–derived signals which enhance both their metastatic and survival potential (Alexander and Friedl, 2012; Hirata et al., 2015; Pickup et al., 2014), including hypoxia-related and/or metabolic stress and adhesion signaling (Hirata et al., 2015; Verduzco et al., 2015; Rahbari et al., 2016). Multiple environmental signals may cooperate to form complex activation networks (Alexander and Friedl, 2012; Domoto et al., 2016); however, genomically and functionally, those evolving tumor subregions that depend on invasive abilities, and account for differential survival and resistance, remain poorly defined.

Cancer invasion occurs through individual or collective cell migration (Nieto et al., 2016; Friedl et al., 2012). Moving single cells detach from the primary site and deliver high numbers of circulating tumor cells with limited probability to survive the metastatic cascade (Smerage et al., 2013; Cheung et al., 2016). Alternatively, collective metastasis empowers grouped cells to invade, circulate, and colonize distant organs with low frequency but high efficacy through cell-to-cell cooperation (Aceto et al., 2014; Cheung et al., 2016). While the particular ability of collective processes for metastatic progression is becoming appreciated, their significance for the therapy response remains unclear (Cheung and Ewald, 2016).

For invasion, tumor cells engage a range of mechanotransduction systems, including integrin-based adhesion systems, which mediate cell–matrix interactions and migration as well as anti-apoptosis and therapy resistance programs (Guo and Giancotti, 2004; Park et al., 2008; Eke et al., 2012; Naci et al., 2012; Ahmed et al., 2013, 2018; Yamaguchi et al., 2015). For example, β1 integrins interacting with fibronectin and other

Check for updates

extracellular matrix (ECM) ligands mediate chemoresistance and resistance to oncogenic BRAF or MAPK/ERK inhibitor treatment (Kanda et al., 2013; Fedorenko et al., 2016; Naci et al., 2012), and expression of αVβ3 integrin in breast, lung, or pancreatic carcinomas characterizes a fraction of cells with stem-like properties that resist tyrosine kinase inhibitors (Seguin et al., 2014). Similarly, disseminated nonproliferating breast cancer cells resort to β1 integrin–dependent survival signaling for long-term persistence (Carlson et al., 2019), suggesting that anti-integrin therapy might reduce metastatic burden and relapse. Integrins or their downstream signaling networks are being explored for overcoming cancer resistance (Vehlow et al., 2016; Raab-Westphal et al., 2017). Single-agent targeting of integrins, however, has failed to reach clinical endpoints in delaying advanced cancers, even in continuous or antibody-based delivery schemes and in combination with cytotoxic therapies (Vehlow et al., 2016; Élez et al., 2015). The resilience of established lesions in both preclinical tumor models and clinical cancers to withstand integrin-targeted therapy may result from compensatory signaling through growth factors and other ECM receptors (Raab-Westphal et al., 2017; Nieto et al., 2016), and further may be supported by cross-talk from multiple integrin subsets and alternative ECM interactions. Integrin expression varies depending on tumor type and tissue context. They may overlap in ligand-binding specificity and coordinate adaptive signaling to promote DNA damage repair, cell survival, and tumor progression (Ahmed et al., 2018; Winograd-Katz et al., 2014; Eke and Cordes, 2015; Janes and Watt, 2004; Hodkinson et al., 2006). Yet their cross-talk in solid tumors and the efficacy of multi-integrin targeting remain unexplored.

To address which tumor regions are especially dependent on integrins for survival and resistance development, we here combined preclinical intravital microscopy with in situ and long-term survival analysis during radiation therapy in orthotopic mouse models of sarcoma and melanoma. We identify collective invasion as a niche for accelerated DNA damage response (DDR) and integrin-dependent radiation resistance. We find that combined β1/αV integrin targeting, but not interference with either integrin subset alone, effectively radiosensitizes and ablates local disease and suppresses metastatic progression.

Results

Collective invasion in orthotopic sarcoma and melanoma xenografts

To identify tumor subregions of therapy resistance and test whether invasion and survival programs coincide, we monitored fluorescent orthotopic HT-1080 sarcoma and MV3 melanoma xenografts in the mouse dermis during invasion and response to preclinical therapy using longitudinal intravital multiphoton microscopy (Alexander et al., 2008). Originating from the growing tumor, both sarcoma and melanoma lesions developed deep invasion of the dermis (mean velocity ∼100 µm/d; Fig. S1, A–C), with >98% of the cells moving collectively, as continuous strands connected to the tumor core, or as detached clusters (Fig. 1, A–C; and Videos 1 and 2). Intact cell–cell junctions and

collective polarity were verified from (i) linear enrichment of the homophilic adhesion receptor ALCAM (CD166) between invading HT-1080 and MV3 cells (Fig. 1 D), (ii) collective front-rear polarity with mitotic planes aligned perpendicular to the invasion direction (Fig. S1 D), and (iii) multicellular orientation along tissue landmarks such as collagen bundles, myofibers, and perfused blood vessels (Fig. 1, B and D; Weigelin et al., 2012). These collective patterns obtained in the mouse model recapitulated the predominantly multicellular strands and nest-like patterns of tumor cells in the invasion zone of clinical sarcoma and melanoma specimens (Fig. S1, E and F; Eyden et al., 1998; Clark et al., 1969).

Collective invasion represents a radioresistant niche

We next addressed whether tumor subregions, including the collective invasion niche, responded differentially to genotoxic therapy. In disseminated clinical sarcoma, DNA-damaging radiotherapy is highly effective; however, patient subsets (10–20%) with advanced tumors develop resistance and/or experience local toxicity and compromised organ function due to high radiation doses (Haas et al., 2015, 2018; Gorayski et al., 2015; Espenel et al., 2017; Guadagnolo et al., 2014). Melanoma requires particularly high cumulative radiation doses, which limits the applicability of radiotherapy in functionally sensitive regions (Mahadevan et al., 2015; Espenel et al., 2017). To reliably eliminate locally advanced or resistant tumors, radioenhancing strategies are being explored preclinically and clinically, among them the use of MEK inhibitors and anti-angiogenic agents (Haas et al., 2015).

As an irradiation (IR) scheme enabling homogeneous and sustained exposure across all tumor regions, isometric whole-field IR and fractionation were applied in invading tumors after the angiogenic switch, as seen by the presence of perfused blood vessels within the tumor core (Fig. 2 A and Fig. S2, A and B). IR has the notable experimental advantage that it avoids pharmacodynamic issues such as varying or inadequate compound delivery to tumor subregions due to heterogeneous vascular perfusion or pressure distribution (Tolaney et al., 2015). IR, by contrast, applies an identical level of genotoxic stress over large tumor regions and so addresses possible heterogeneities in locoregional response. Fractionated IR induced mitotic arrest within hours in both the tumor core and the invasion zone, followed by cell death (Fig. 2, B and C; and Fig. S2, C and E) and substantial tumor regression a few days later (Fig. 2, D and E; and Fig. S2, F and G). Cell death was identified by three-dimensional (3D) intravital reconstruction and single-cell analysis of nuclear fragmentation and/or disappearance of the cytoplasmic label in vivo (Fig. 2, B and G). After IR in vitro, nuclear fragmentation coincided with positive staining for cleaved caspase-3 in organotypic invasion culture (Fig. S2 H). Despite overall tumor regression, induction of cell death varied significantly between different regions of the tumor. Whereas background levels of nuclear fragmentation in untreated mice were similar between the tumor core and the invasion zone, nuclear fragmentation in the tumor core was elevated at least fourfold but tended to only mildly increase, by twofold, in the invasion zone (Fig. 2, B–D; and Fig. S2, D and E). As a
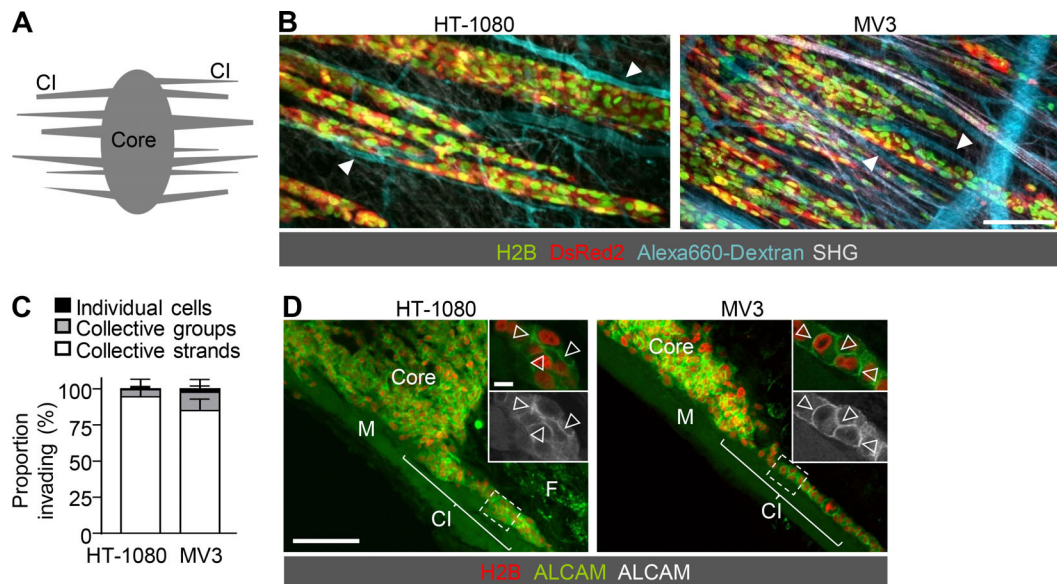
Figure 1. Collective invasion as primary invasion pattern in sarcoma and melanoma xenografts. (A) Schematic view defining tumor core and collective invasion zone (CI) of tumors growing in the deep dermis of the mouse monitored intravitally through an imaging window. **(B)** Collective invasion strands of human HT-1080 sarcoma (left; day 7; see also Video 1) and MV3 melanoma xenografts (right; day 8; see also Video 2). Tumor cells stably express nuclear H2B-EGFP and cytoplasmic DsRed2. Alexa Fluor 660–conjugated dextran contrastsperfused blood vessels. Second harmonic generation (SHG) visualizes muscle and collagen fibers. Arrowheads, alignment of invasion strands with perfused blood vessels. Scale bar, 100 μm. **(C)** Prevalence of invasion types, including individual cells, detached clusters, or collective strands connected to the core (day 5–7). Data represent the means and SD from five (HT-1080) and three (MV3) tumors. Per tumor, on average 150 (HT-1080) and 300 (MV3) cells were analyzed. **(D)** Distribution of ALCAM along cell–cell junctions (arrowheads) in invading tumor strands. Maximum-intensity projections (overview) and individual sections (insets) from confocal 3D stacks. Diffuse background fluorescence originates from fat (F) and myofibers (M). Scale bars, 100 μm (overview); 10 μm (insets).

consequence, with time, invading cells tended to survive or marginally expanded, whereas the core regressed (Fig. 2 F). Time-gated quantification of the surviving subsets in HT-1080 tumors showed that at 8 d after IR, when there was profound regression of the tumor core, in the invasion zone >99% of the cells survived in collective invasion strands and clusters, based on cytoplasmic DsRed2 signal (Fig. 2 G, green label) and intact nuclei (Video 3). Conversely, the frequency of solitary invasive cells decreased from day 6 to 14 from 1.4 ± 1.1% to 0.7 ± 0.7% (Fig. 2 G), indicating that the rare single cells disseminating in vivo are at least twofold less likely to survive after IR compared with grouped cells. These data strongly indicate that collective invasion is a niche for relative radioresistance in an otherwise radiosensitive tumor.

Accelerated DDR in the invasion niche

In brain tumors, tumor cell invasion was reported to associate with decreased cell proliferation, which could account for increased resistance toward DNA-damaging radiation therapy (Giese et al., 1996; Roth et al., 2000; Hsu et al., 1962). However, both HT-1080 and MV3 melanoma models show similar proliferation in the invasion zones of untreated tumors and similarly undergo mitosis arrest during fractionated IR (Fig. S2, C and E). This suggests that cell cycle–dependent effects may not support preferential survival of the invasion niche. Instead, cells in the two subregions might deal differentially with the radiotherapy-induced damage. IR causes DNA double-strand breaks (DSBs), followed by a DDR with DNA repair or apoptosis induction as

outcomes (Ciccia and Elledge, 2010; Zannini et al., 2014). To explore whether the tumor core and the invading niche differ in their DDR, we performed quantitative subregion analysis of central DDR effectors in untreated and irradiated lesions (Fig. 3, A–C; and Fig. S3, A–E). Both HT-1080 and MV3 cells express wild-type P53 (Tarunina and Jenkins, 1993; Houben et al., 2011) and thus are competent to undergo cell cycle arrest and DNA repair after DNA damage (Ciccia and Elledge, 2010). 30–60 min after IR, the general DSB marker γH2AX (Rogakou et al., 1998) was induced with equal (HT-1080) or mildly increased (MV3) levels in the invasion zone relative to the core (Fig. 3, D and E; and Fig. S3 F). This indicates uniform initiation of the DDR across the tumor. The low γH2AX baseline in invading cells rules out preset DSB elevation possibly induced by mechanical damage of the nucleus during collective invasion (Denais et al., 2016) or other microenvironmental assault, e.g., by reactive oxygen species (Martinez-Outschoorn et al., 2010; Radisky et al., 2005). CHK2 phosphorylation, which activates CHK2 and controls DDR outcome (Zannini et al., 2014), was similar in all tumor regions shortly after IR and reverted to baseline in the collective invasion zone 1 d later but remained elevated in the tumor core (Fig. 3, D and E; and Fig. S3, F and G). Similarly, phosphorylated ATM/ATR substrates, which also include CHK2, P53, BRCA1 and further effectors (Zannini et al., 2014; Shiloh and Ziv, 2013), decreased in the invasion zone of HT-1080 lesions after 24 h but remained elevated in the core (Fig. 3 E). CHK2 kinase has a dual role in the DDR, including induction of cell cycle arrest, which supports DSB repair, or induction of apoptosis in case damage is
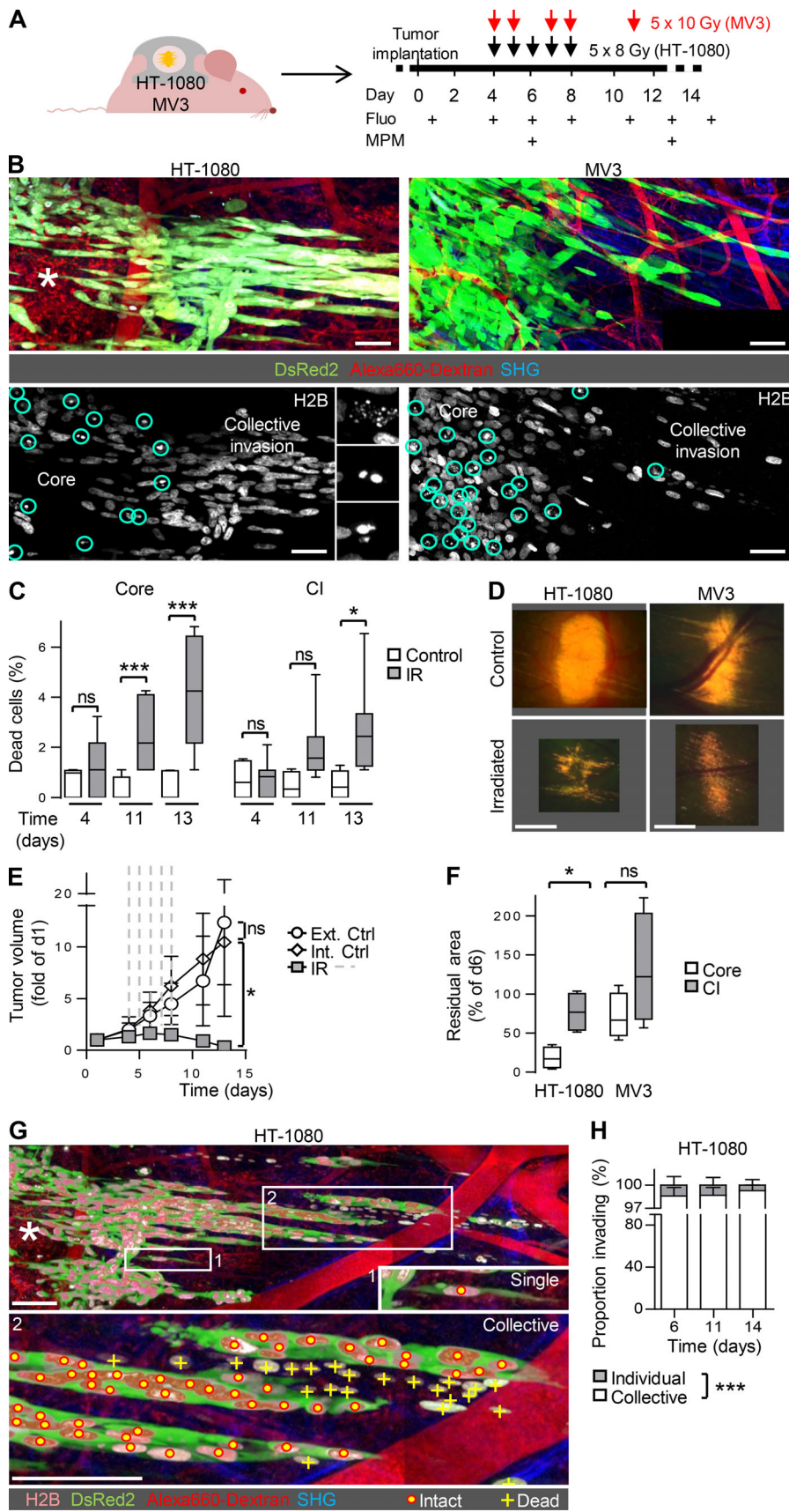
A

B

HT-1080   MV3

DsRed2   Alexa660-Dextran   SHG

Figure 2. Collective invasion niche mediates radioresistance. (A) Experimental procedure for sequential intravital imaging of the tumor response to fractionated IR. Fluo, epifluorescence overview microscopy. MPM, subcellular-resolved multiphoton microscopy. **(B)** Differential response to radiation therapy in invasion strands and tumor core. Multiphoton microscopy images show the borders between core and collective invasion zone (day 13). Black box in lower right corner (MV3) results from stitching of adjacent images without complete overlap. Asterisk, regressing tumor core. Circles and insets in lower panel, nuclear fragmentation used for quantification of dead cells. Scale bars, 50 µm. **(C)** Frequency of fragmented nuclei indicating dead cells in HT-1080 tumor cores and collective invasion strands. Data represent medians, 25th/75th percentiles (box), and 5th/95th percentiles (whiskers) of ~80 nuclei per tumor region from 5–20 fields/tumor from three to four independent mice. *, P = 0.005; ***, P < 0.0001; ns, not significant. Statistics, Mann–Whitney U test (Bonferroni-corrected threshold: P = 0.008). **(D)** Epifluorescence overviews of whole-tumor topology in untreated and irradiated HT-1080 (5 × 8 Gy) and MV3 (5 × 10 Gy) lesions (day 13). Images are derived from Fig. S1 A (control) and Fig. S2 G (irradiated). Scale bar, 1 mm. **(E)** HT-1080 tumor growth before, during (dashed lines; 5 × 8 Gy), and after IR, compared with untreated tumors in independent mice (Ext Ctrl) or nonirradiated contralateral tumors in the same mouse (Int Ctrl). Means ± SD (three to nine independent tumors). *, P = 0.02 (difference between irradiated and control tumors at the endpoint [day 13]). Statistics, Mann–Whitney U test. **(F)** Extent of tumor regression in core and invasion zone of irradiated tumors. Data show median residual areas, 25th/75th percentiles (box), and 5th/95th percentiles (whiskers) of day 13 normalized to day 6 from four independent tumors per condition. *, P = 0.03. Statistics, paired t test. **(G)** Collective survival niche after IR. Multiphoton microscopy image shows the border between core and invasion zone of an irradiated HT-1080 tumor (day 14). Persisting, invading cells were quantified as individual or collective cell patterns connected by the DsRed2-positive cytosol. Dead cells were lacking cytoplasmic signal. Asterisk, regressing tumor core. Scale bars, 100 µm. **(H)** Classification of surviving, invading cells based on the migration pattern, including individual cells or collective strands. Data represent the means and SD from three tumors (HT-1080). ***, P < 0.0001. Statistics, paired t test.
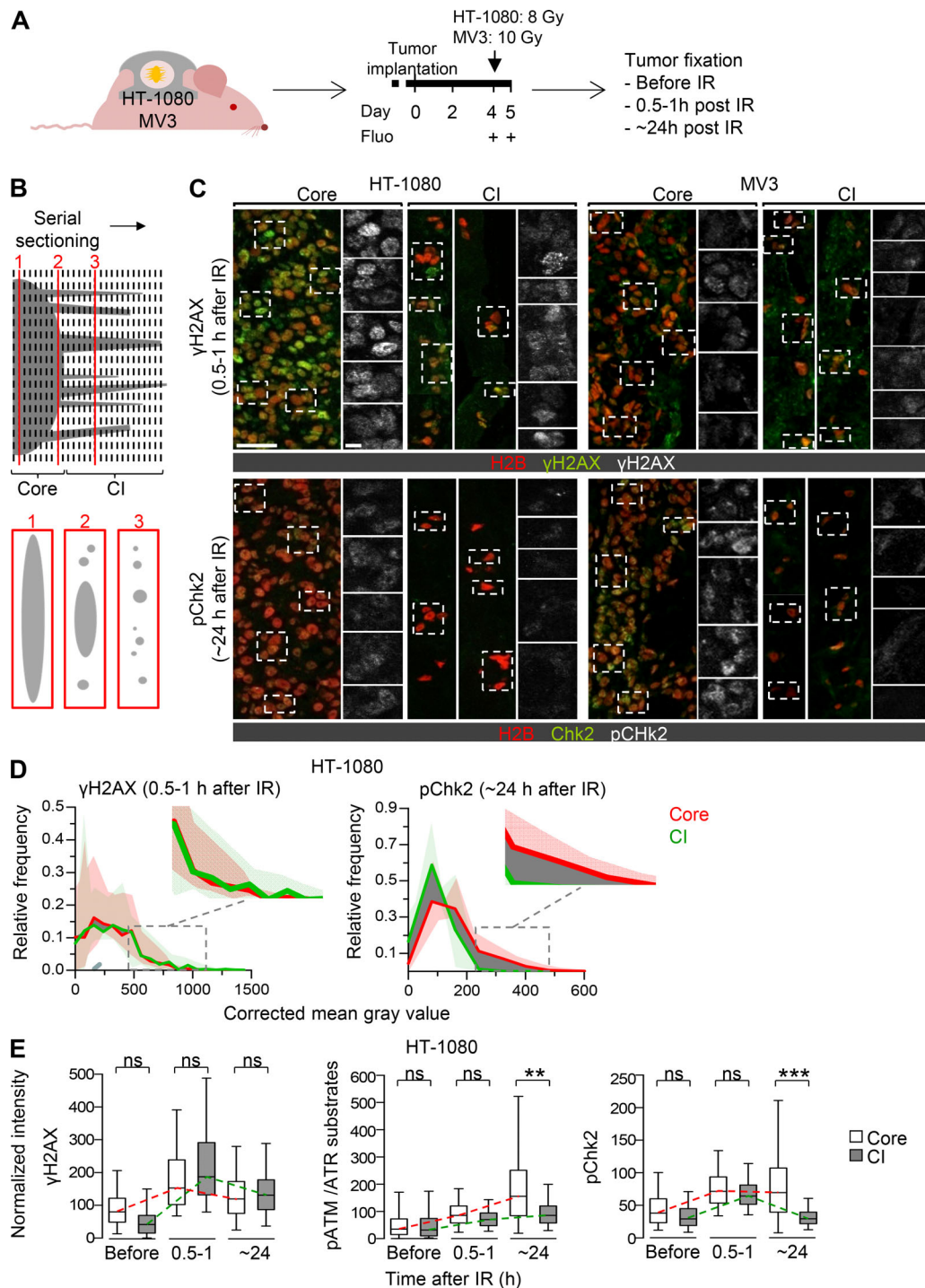
C

D

E

F

G   HT-1080

H2B   DsRed2   Alexa660-Dextran   SHG   • Intact   + Dead

H

Figure 3. **Differential DDR in tumor core and collective invasion niche. (A)** Experimental procedure for tumor sample collection to analyze the DDR. Fluo, epifluorescence overview microscopy. **(B)** Strategy for differential immunohistological analysis of DDR in tumor core and collective invasion (CI) zone. Upper panel, serial sectioning of the entire tumor; lower panels, resulting cross-sectioned patterns. **(C)** γH2AX and pChk2 signal in tumor core and collective invasion zone detected at early (≤1 h) and late (24 h) time point after a single-dose IR. Maximum-intensity projections from confocal 3D stacks. Dashed rectangles indicate representative tumor nuclei for single-channel display of γH2AX or pChk2 signal. H2B, H2B-EGFP (tumor nuclei). Images were chosen to show the variation of the intensity and subcellular structure of positive events. Scale bars, 50 µm (overview); 25 µm (inset). Examples for nonirradiated samples are shown in Fig. S3 E. **(D)** Intensity distribution of DDR signals in HT-1080 tumors after a single-dose IR. Data show the mean gray value after background correction (lines) and signal range (filled areas, lowest to highest values) from three independent tumors. Dark gray shaded area, difference between core and collective invasion zone. **(E)** Quantification of γH2AX, pATM/ATR substrates, and pChk2 signal intensity after single-dose IR. Data represent the median gray value per nucleus after background correction, with 25th/75th (box) and 5th/95th percentiles (whiskers) from three independent tumors. ~150–600 nuclei per invasion zone and tumor and ~1,000–6,000 representative nuclei per core and tumor were analyzed. Dashed lines visualize approximate dynamics of DDR. **, P = 0.003; ***, P < 0.0001. Statistics, mixed-model ANOVA (see Materials and methods for details).

irreparable (Zannini et al., 2014). Thus, the observed prolonged CHK2 phosphorylation (Fig. 3 E and Fig. S3 F) in association with local regression of the core (Fig. 2, B and F) suggests that persisting irreparable DNA damage is associated with cell death. Conversely, timely normalization of Chk2 activity followed by cell survival in the collective invasion niche indicates an efficient repair of DNA damage (Fig. 2, B and F).

Combined β1 and β3 integrin functions underlie invasion-associated radioresistance

When we probed for vascular integrity by assessing the retention of intravascular dextran (Fig. 1 B and Fig. 2 B), or for tissue hypoxia using pimonidazole staining (Fig. S1 G), we found that invading sarcoma and melanoma cells engaged with morphologically intact, well-perfused, and metabolically unperturbed dermal stroma. These results suggest that hypoxia-mediated resistance is unlikely (Verduzco et al., 2015). We therefore tested whether integrins, which are expressed and engaged during collective invasion (Yamaguchi et al., 2015; Hegerfeldt et al., 2002) and have been implicated in mediating radioresistance (Park et al., 2008; Monferran et al., 2008; Eke et al., 2012; Mikkelsen et al., 2009), also orchestrate tumor cell survival during invasion in vivo. HT-1080 and MV3 cells expressed high levels of β1 integrin and low to moderate levels of β3 and β5 integrin and lacked other β integrin subsets (Fig. S4, A and B). We initially focused on the function of β1 and β3 integrins in mediating survival during collective invasion, based on their established role in mediating radioresistance in primary and metastatic cancer models (Yamaguchi et al., 2015; Park et al., 2008; Eke et al., 2012; Ahmed et al., 2013, 2018; Guo and Giancotti, 2004). β1 Integrins alone or, to account for potential compensation, together with β3 integrins, were downregulated in HT-1080 cells by stable RNA interference (RNAi), yielding ∼80% reduction of extracellular β1 integrin expression (Fig. S4, C–E). The remaining β1 integrin level was sufficient to maintain cellular attachment, and no major growth deficit was noted during propagation in cell culture (data not shown); this minimizes the risk for a culture-based selection bias toward cell reprogramming to integrin and anchorage independence (Cerezo et al., 2009). To maximize inhibition in vivo and target residual β1 integrin chains, mice carrying HT-1080 shRNA-expressing tumors additionally received human-selective anti-β1 integrin antibody 4B4 (Fig. 4 A; Takada and Puzon, 1993). This regimen repressed the β1 adhesion epitope by nearly 100% in vitro (Fig. S4 F). In nonirradiated HT-1080 tumors, β1 and β1/β3 integrin interference arrested mitosis, enhanced cell death, and retarded growth in the tumor core (Fig. 4, B–D), similar to effects on epithelial tumors and glioma (Park et al., 2008; Eke et al., 2012; Ahmed et al., 2013, 2018; Carbonell et al., 2013). In situ MAPK signaling, which supports cell growth and survival downstream of integrins (Eke and Cordes, 2015), was diminished after β1/β3 integrin targeting to levels slightly below the stromal background (Fig. S4 G). Notably after integrin targeting, the tumor core regressed, whereas the collective invasion zone retained low-level mitotic activity and persisted beyond day 13; however, with increased detachment of cell groups and individual cells as also previously shown in vitro (Hegerfeldt et al., 2002; Fig. 4, B,

E, and F). The early-onset induction of cell death by mono- versus dual-integrin targeting was comparable (Fig. 4 C); however, at later time points, marginally significantly enhanced regression of both the tumor core and invasion zone was achieved by dual targeting (Fig. 4 D).

This indicates that the collective invasion niche withstands anoikis induction after integrin deprivation by, e.g., acquiring an anchorage-independent survival advantage (Paoli et al., 2013; Gibert and Mehlen, 2015). This survival advantage, however, was abrogated when β1 integrin targeting was combined with fractionated IR, disrupting and shrinking the invasion zone (Fig. 5, A and B). This effect was further 20-fold enhanced when β1 and β3 integrins were simultaneously inhibited, reaching effective regression of both the tumor core and collective invasion niche within 3–5 d (Fig. 5, B–D). Since dual β1/β3 integrin targeting was superior to β1 integrin monotargeting in radiosensitizing HT-1080 tumors, both integrins likely cooperate to enhance cancer cell survival in invading cells.

Antibody-based dual β1 and αV integrin targeting to overcome radioresistance

To verify these findings using a translational approach, and to effectively target all expressed integrin subsets, including β1, αVβ3, and αVβ5, multiple-integrin targeting was applied to HT-1080 and MV3 tumors by systemic antibody application before and during radiotherapy (Fig. 6 A). To interfere with αV integrins on tumor cells and simultaneously target αVβ3 and αVβ5 integrins while avoiding interference with αIIbβ3 integrin expressed by platelets, which can induce bleeding as a side effect (Hodivala-Dilke et al., 1999), we used human-selective anti-αV integrin antibody 17E6, which selectively interferes with all αV integrins (Fig. S4, A and B; Mitjans et al., 1995). When combined with IR, antibody-based β1/αV integrin targeting induced rapid and severe cell death followed by regression of the entire lesion in both tumor types (Fig. 6, B and C; and Fig. S5, A–C). By day 7 after IR, HT-1080 tumor remnants consisted of few individualized nondividing and slowly regressing cells in perivascular position, of which very few cells persisted until day 28, when animal welfare required termination of intravital monitoring (Fig. 6, B and D; and Fig. S5, A, D, and E). Likewise, both tumor core and invasion strands of MV3 lesions effectively regressed with mitotically inactive scattered cells as remnants (Fig. 6, B and D; and Fig. S5, D and E). The notable difference in regression kinetics between the two tumor models replicates the higher radiation sensitivity of clinical sarcoma compared with melanoma (Gorayski et al., 2015; Hoefkens et al., 2016). These data indicate that combining antibody-based β1 and αVβ3/β5 integrin targeting overcomes invasion-associated radioresistance and ablates the collective invasion niche.

To address the radiosensitizing impact of single- versus multiple-integrin targeting for long-term survival, fluorescent HT-1080 and MV3 tumors were implanted into the imaging window–free dermis under ultrasound control and followed for 180 d (Fig. 7, A and B; and Fig. S5 F). Mice bearing emerging macroscopic and exponentially growing tumors were treated with antibodies 4B4 and 17E6, individually or combined, and irradiated using an adjusted, dose-conservative scheme
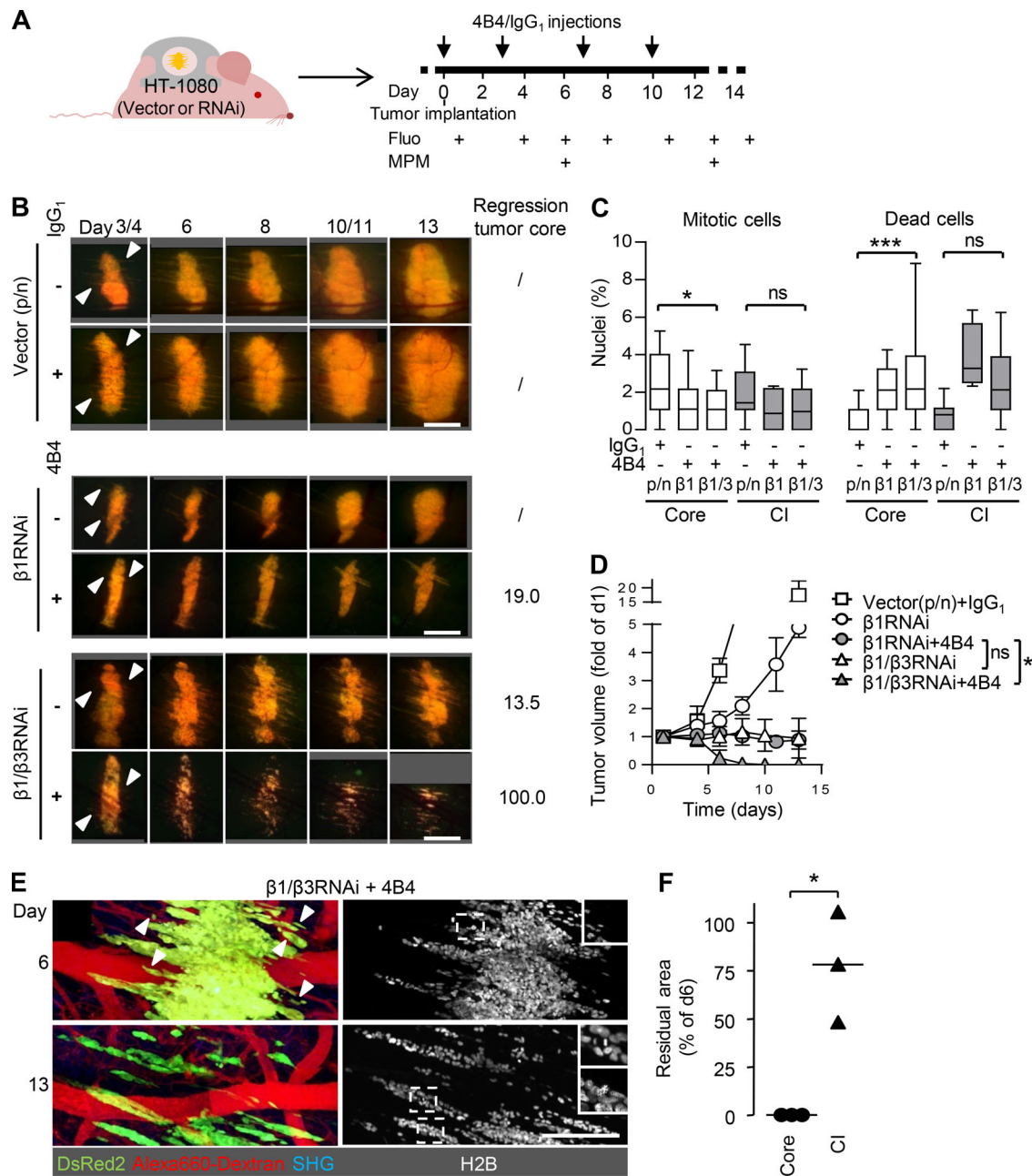
Figure 4. Compromised tumor integrity and persistence of the invasion niche by RNAi- and antibody-based targeting of β1/β3 integrins in HT-1080 tumors. (A) Experimental procedure for administration of anti-β1 integrin mAb 4B4 or IgG1 and sequential intravital microscopy of the tumor response to integrin interference. Fluo, epifluorescence overview microscopy. MPM, subcellular-resolved multiphoton microscopy. **(B)** Time course of tumor growth or regression in control tumors transduced with empty vectors (p-puro/p-neo), β1RNAi or β1/β3RNAi in the absence or presence of IgG1 or anti-β1 integrin mAb 4B4. White arrowheads, onset of collective invasion. Numbers (right column), percentage mean regression of the tumor core (day 13 compared with day 6) from three to four independent tumors. Scale bars, 1 mm. **(C)** Fractions of mitotic and dead cells (day 6) quantified based on nuclear morphology for different interference schemes displayed as medians, 25th/75th percentiles (box), and 5th/95th percentiles (whiskers) from 20 independent fields from three to four independent tumors. Per condition, 19–20 nuclei were analyzed for the core and ~10 nuclei for the invasion zone. *, P = 0.01; ***, P < 0.0001; ns, not significant. Statistics, Mann–Whitney *U* test (Bonferroni-corrected threshold: P = 0.0125). **(D)** Tumor development in response to the indicated interference procedures. Data show the means ± SD from three to four independent tumors. *, P = 0.0286. Statistics, Mann–Whitney *U* test. **(E)** Preferential survival of invading collective strands after combined β1/β3 integrin targeting. Z-projections of the same tumor region. Black box in upper left corner (day 6) results from stitching of adjacent images without complete overlap. Insets, mitotic figures in collective strands. Arrowheads, detachment of cell groups and individualized cells. Scale bar, 250 μm. **(F)** Median residual volume of tumor core and collective invasion (CI) zones after β1/β3RNAi combined with mAb 4B4 (day 13 compared with day 6) from three independent tumors. *, P < 0.05. Statistics, paired *t* test.

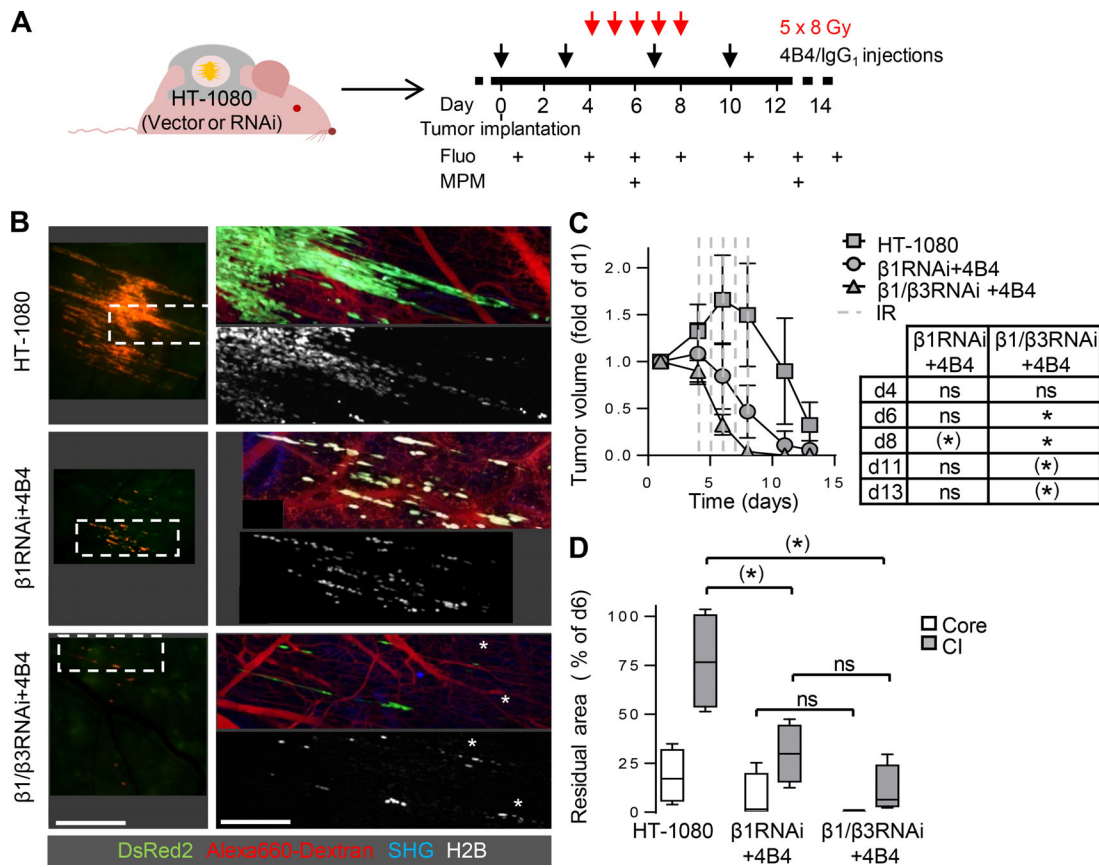Figure 5. **Radiosensitization of HT-1080 tumors by β1/β3 integrin RNA interference combined with antibody-based β1 integrin targeting. (A)** Protocol for administration of anti-β1 (4B4) or IgG1 combined with fractionated IR and sequential intravital imaging of the tumor response. Fluo, epifluorescence overview microscopy. MPM, subcellular-resolved multiphoton microscopy. **(B)** Topology and extent of the invasion zone in response to fractionated IR combined with single-integrin (β1) or dual β1/β3 integrin interference. Epifluorescence (left) and 3D reconstructed z-projections from regions marked by dashed boxes using multiphoton microscopy (right; day 13). White asterisks, apoptotic nuclei. Scale bars, 1 mm (left); 250 µm (right). **(C)** Time-dependent tumor volume. Data show the means ± SD from three to four independent tumors, with P values for comparing irradiated integrin-targeted tumors to irradiated control tumors. (*), P = 0.006; *, P = 0.004. Statistics, Mann–Whitney U test (Bonferroni-corrected threshold: P = 0.005). **(D)** Regression of tumor core and collective invasion (CI) zone after IR with or without integrin mono- or dual interference. Data show median residual areas, 25th/75th percentiles (box), and 5th/95th percentiles (whiskers) of day 13 normalized to day 6. Per condition, four tumors were analyzed. (*), P = 0.03; ns, not significant. Statistics, Mann–Whitney U test (Bonferroni-corrected threshold: P = 0.0125).

(cumulative 10–15 Gy) to achieve relapsing disease in 70–80% of the cohort receiving nontargeting IgG1 isotypic control antibody (Fig. 7, A and D; and Fig. S5 G). To account for minimal residual and metastatic disease, both tumor implantation site and distant organs were dissected at the endpoint post mortem and assessed for the presence of (disseminated) tumor cells (Fig. S5, H–J). Tumors in window-free mice developed collective invasion as a primary pattern (Fig. 7 C), ruling out artifacts caused by the imaging window.

In contrast to the RNAi-based and early-onset antibody treatment in small tumors, which was used to target integrins for intravital multiphoton microscopy (compare Figs. 4 and 6), antibody-based targeting of β1 and αV integrins without IR in exponentially growing, established tumors did not provide a relevant survival advantage. Upon radiotherapy, multiple-integrin targeting significantly improved the radiation response, resulting in local relapse-free outcome and overall survival in 80% (HT-1080) and >90% (MV3) of the mice (Fig. 7 D and Tables S1 and S2). Individual targeting of either β1 or αV integrins failed

to substantially increase overall survival after IR (Fig. 7 D), similar to relapsing disease after integrin monotargeting in epithelial and glioma cancer models (Carbonell et al., 2013; Ahmed et al., 2013). In addition, 90% (HT-1080) and 100% (MV3) of the mice receiving IR plus multiple-integrin targeting were free of distant metastases (Tables S1 and S2). This lack of distant metastasis in most mice suggests that cells were lethally damaged and failed to exit the primary site. Alternatively, surviving cells, after leaving the site of therapy, may have reached the lungs and reside with long-term cell cycle arrest but fail to mount metastatic outgrowth (Gérard and Goldbeter, 2014).

Discussion

These data identify mesenchymal collective invasion as a niche for acquired radioresistance in vivo. We used human sarcoma and melanoma models targeted by stable RNAi or human-selective anti-integrin antibodies (Mahalingam et al., 2014; Takada and Puzon, 1993; Mitjans et al., 1995), thereby ignoring
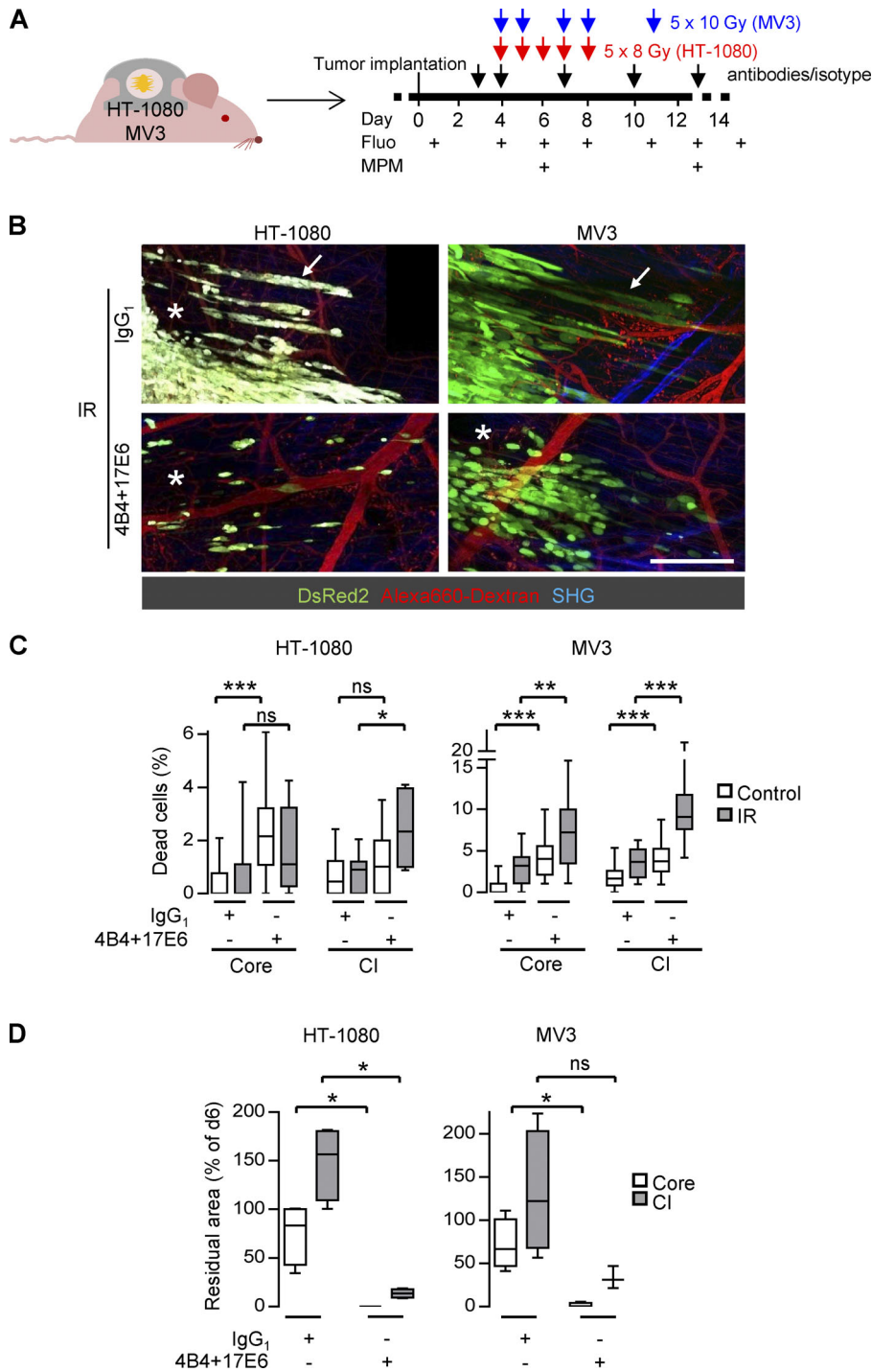
Figure 6. **Dual-integrin targeting abrogates radioresistance in the collective invasion niche. (A)** Protocol for administration of anti-β1 (4B4) and αV integrin (17E6) mAbs or IgG1 combined with fractionated IR and sequential intravital imaging of the tumor response. Fluo, epifluorescence overview microscopy. MPM, subcellular-resolved multiphoton microscopy. **(B)** Radiation response of tumor core and collective invasion zone after combined treatment with mAbs 4B4 and 17E6 compared with IgG1-treated control (day 13). Black box in upper right corner (HT-1080, IgG1) results from stitching of adjacent images without complete overlap. Asterisks, areas of regression. Arrows, persisting invasion strands. Alexa Fluor 660–conjugated dextran-perfused blood vessels. Second harmonic generation (SHG) originates from muscle and collagen fibers. Scale bar, 250 μm. **(C)** Frequency of dead cells in core and collective invasion (CI) zone after antibody-based integrin targeting and/or IR (day 6). Data show the medians, 25th/75th percentiles (box), and 5th/95th percentiles (whiskers) of ~20 nuclei per condition and tumor regions from four to five tumors, reflecting a total of 9–28 different microscopic fields. *, $P = 0.01$; **, $P = 0.001$; ***, $P < 0.0001$; ns, not significant. Statistics, Mann–Whitney U test (Bonferroni-corrected threshold: $P = 0.0125$). **(D)** Extent of tumor regression in core and collective invasion zone of irradiated tumors combined with or without integrin targeting. Data show median residual areas, 25th/75th percentiles (box), and 5th/95th percentiles (whiskers) of day 13 normalized to day 6 from four independent tumors. *, $P = 0.03$. Statistics, Mann–Whitney U test.

any direct role of integrins present in the murine tumor microenvironment. These data reveal integrin-mediated resistance as a tumor-cell intrinsic process arising with connective tissue invasion (Mahalingam et al., 2014; Takada and Puzon, 1993; Alexander and Friedl, 2012), which differs from stromal reprogramming by integrin adhesome–dependent signaling during molecular targeted therapy (Hirata et al., 2015) or tumor growth reduction after interference with vascular integrins (Tolaney et al., 2015). β1 and αV integrin engagement in the deep dermis is likely mediated by their connective tissue ligands,

collagens, laminins, fibronectins, vitronectin, and Cyr61 (Gibert and Mehlen, 2015; Weigelin et al., 2012; Mauger et al., 1987; Chen et al., 2000; Dahlbäck et al., 1993). In contrast to hypoxia-mediated metabolically induced cancer resistance (Verduzco et al., 2015), the invasion niche is normoxic, therefore we considered hypoxia-mediated resistance programs as unlikely. Functional blockade of β1 integrins in explant culture has been shown to induce disruption of collective invasion and transition to single-cell dissemination (Hegerfeldt et al., 2002), and a trend to increased fragmentation of the collective invasion zone after
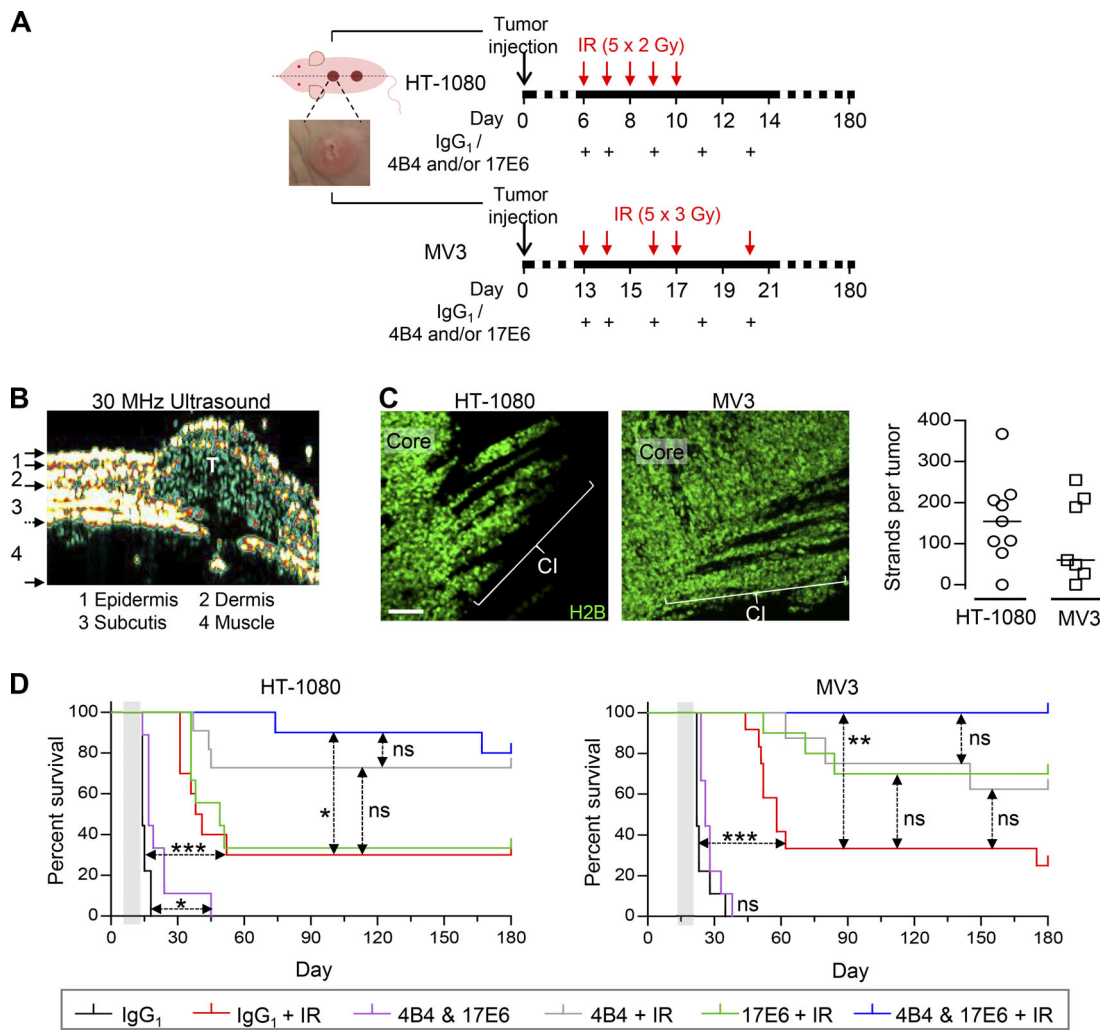
Figure 7. Dual-targeted but not individual anti-integrin therapy to enhance radiation response, tumor eradication, and long-term survival. (A) Treatment schemes for HT-1080 and MV3 tumors. Tumor cells were injected at day 0, resulting in an intradermally growing tumor located along the dorsal midline (dashed line). Example image, intradermal HT-1080 lesion. Time points of IR and antibody administration are indicated. **(B)** Tumor lesion (T) after implantation in imaging window–free mouse. Intradermal localization was confirmed by high-frequency ultrasound. **(C)** Collective invasion (CI) pattern in intradermal tumors in imaging window–free dermis (maximum-intensity projections). Number of multicellular strands per tumor was counted from 50-µm-thick tumor sections from nine (HT-1080) and seven (MV3) tumors. Scale bar, 100 µm. **(D)** Tumor-free overall survival of mice after application of treatment, including fractionated IR without and with individual and dual-targeted integrin inhibition with antibodies 4B4 and/or 17E6, compared with IR combined with isotypic control antibody (representing IR alone without integrin targeting). Mice were sacrificed after 180 d or earlier, upon humane endpoint criteria (tumor size of 2 cm³, ulceration, weight loss, or poor overall condition due to internal metastasis). See Table S1 for details on mouse numbers (8–12 mice per group), metastasis formation, and tumor remnants. Gray-shaded area, therapy phase. *, P = 0.01; **, P = 0.0003; ***, P < 0.0001; ns, not significant. Statistics, log-rank survival analysis (Bonferroni-corrected thresholds: P = 0.01 [HT-1080] and P = 0.008 [MV3]).

combined β1 and αV integrin targeting was notable in vivo; however, the majority of cells retained their collective invasion pattern after integrin inhibition and IR, and additional strand fragmentation may have occurred due to cell death. Therefore, integrin targeting lowered the survival ability of the collective invasion niche.

Integrin-mediated growth and survival signaling in response to interaction with ECM has been identified in a range of epithelial and mesenchymal tumors (Babel et al., 2017; Ahmed et al., 2018; Leith et al., 2018). The integrin adhesome comprises a complex, multisignal downstream network. This involves the activation of focal adhesion kinase (FAK), Src, integrin-linked kinase, and PINCH1, that then trigger and synergize with MAPK

and phosphoinositide 3-kinase signaling and downstream effectors, including MYC and NF-κB (Eke et al., 2012; Monferran et al., 2008; Seguin et al., 2015; Winograd-Katz et al., 2014; Eke and Cordes, 2015; Hodkinson et al., 2006; Janes and Watt, 2004). Additional noncanonical effectors of integrin signaling further include cross-talk with the CD44/hyaluronic acid axis, epidermal growth factor (EGF) receptor, and syndecan signaling (Yu et al., 2000; Ghatak et al., 2014; McQuade et al., 2006). In head and neck squamous cell carcinoma cells, β1 integrin activating FAK/JNK1 is essential for the repair of radiation-induced DSBs, and β1 integrin signaling supports expression of essential DNA repair genes, including Ku70/80 and Rad51 (Dickreuter et al., 2016; Ahmed et al., 2018). These data link integrin signaling to

the major DSB repair pathways, nonhomologous end joining and homologous recombination. However, the exact repair mechanisms and precise signaling pathways that, downstream of integrins, support accelerated DNA damage repair and may therefore account for resistance of the invasion niche in mesenchymal sarcoma and melanoma tumors remain to be identified by future research.

By directly targeting integrin receptors upstream of the signaling network, even moderate IR (cumulative doses of 10 to 15 Gy) entirely eliminated the tumor and prevented systemic micro- or macrometastasis. This indicates that targeting β1/αV integrin upstream can reach particular efficacy in nonredundantly perturbing the integrin adhesome and downstream signaling, whereas interference with signaling intermediates downstream of integrins (e.g., FAK, Src, MAPK) may trigger network rewiring and development of resistance (Wellbrock and Arozarena, 2016; Hirata et al., 2015; Vehlow et al., 2016).

Most known integrins and their downstream signaling have been, individually and largely unsuccessfully, pursued for therapeutic intervention (Raab-Westphal et al., 2017). Preclinical efficacy of inhibiting individual integrins is commonly incomplete in strength and/or duration (Kim et al., 2016; Élez et al., 2015; Raab-Westphal et al., 2017; Vehlow et al., 2016), and cells expressing multiple integrins may generate compensatory signaling by switching their integrin dependence (Janes and Watt, 2004). In mesenchymal sarcoma and melanoma tumors, β1/αV dual targeting, but not interference with either subset alone, was sufficient to revert radioresistance in the invasion niche. This combination potentially targets 15 of 16 integrin members expressed by mesenchymal and epithelial tumor cells and previously tested in clinical trials, including α1-11β1, αVβ3, αVβ5, αVβ6, and αVβ8 (Raab-Westphal et al., 2017). In carcinomas, α6β4 and α6β7 integrins may mediate additional cross-talk (Lu et al., 2008) and require cotargeting to minimize resistance.

Importantly, for application in patients, future work needs to secure the tolerability and applicability of combined β1/αV integrin targeting. Pan-αV integrin antagonists are clinically well tolerated (Vehlow et al., 2016). Although not shown to be toxic in mice (Park et al., 2006), targeting of β1 integrin, due to its ubiquitous expression and pleiotropic functions, may require particular caution, including time-restricted or intermittent dosing and possibly preventive care to minimize leukocyte malfunction or wound healing defects (Koivisto et al., 2014). Clinical indications for combining multiple-integrin targeting with radiotherapy particularly include perisurgery therapy of advanced or deeply infiltrative tumors, to reduce local relapse and surgery-induced systemic dissemination (Burmeister et al., 2012; Jatana et al., 2016). Other indications may include relapsing disease after radiation therapy and lowering radiation dose to prevent loss of functionality of tissues susceptible to radiation injury (e.g., head and neck region, axilla; Kris et al., 2017). Besides radiosensitization, multiple-integrin inhibition may also reduce resistance to chemotherapies and molecular targeted therapies (Naci et al., 2015; Hirata et al., 2015). Combining antibody-based integrin targeting with IR or chemotherapy may boost both tumor-cell death and, via opsonization, tumor-

antigen uptake by phagocytes and augment checkpoint targeted immunotherapy (Formenti and Demaria, 2013). In conclusion, multi-integrin–targeted therapy provides rational opportunities to improve DNA damaging therapy and eradicate niches of tumor resistance in clinical settings.

Materials and methods
Cells and cell culture
Human HT-1080 sarcoma (Rasheed et al., 1974) and MV3 melanoma cells (van Muijen et al., 1991) were cultured in DMEM (PAN Biotech or Invitrogen) supplemented with 10% FCS (Aurion or Sigma-Aldrich), penicillin, and streptomycin (both 100 µg/ml; PAN Biotech or PAA Laboratories) at 37°C in a humidified 5% CO_2 atmosphere. Identity of the cells was verified by SNP_ID Assay (Sequenom, MassArray System, Characterized Cell Line Core Facility, MD Anderson Cancer Center, Houston, TX), and lack of contamination with mycoplasma was routinely verified using the MycoAlert Mycoplasma Detection Kit (Lonza). Dual-color variants of HT-1080 and MV3 cells, expressing cytoplasmic DsRed2 and nuclear histone 2B (H2B)-EGFP (Yamamoto et al., 2004), were cultured in medium additionally containing hygromycin B (0.2 mg/ml; Invitrogen) and G418 sulfate (0.2 mg/ml; Calbiochem).

Generation of stable knockdown cell lines by lentiviral shRNA
ShRNA sequences targeting ITGB1 (β1 integrin, 5′-AGCCACAGA CATTTACATTAAA-3′) and ITGB3 (β3 integrin, 5′-AAGTCACTT TCTTCTTCTTAAA-3′) for gene silencing by RNAi were cloned into the lentiviral vector pLBM containing either a puromycin (p-puro) or a neomycin (p-neo) cassette, and lentiviral particles were produced and concentrated by ultracentrifugation, as described (Kissler et al., 2006). HT-1080 dual-color cells were infected with p-puro or p-neo viruses (vector controls), or with ITGB1 (on p-puro) or ITGB3 targeting (on p-neo) pLBM viruses. For generation of double knockdown cells, HT-1080 p-puro or HT-1080 β1RNAi cells were additionally infected with ITGB3 targeting or p-neo viruses, respectively. Efficiency of protein downregulation was measured by Western blot (β1 integrin) and flow cytometry (β1 and β3 integrin), showing ~80% reduction for β1 integrin and ~90% downregulation for β3 integrin (Fig. S4, C–E). For maintaining stable HT-1080 knockdown cells, medium was supplemented with puromycin (5 µg/ml; Sigma-Aldrich) for single transfectants (single-vector control, β1RNAi) or puromycin and G418 sulfate (400 µg/ml) for dual transfectants (dual-vector control, β1/β3RNAi). Stability of knockdown without antibiotics selection was confirmed after 4-wk culture in antibiotic-free medium and before implantation into mice.

Animal experiments
All animal procedures were approved by the German regional government (Regierung von Unterfranken; TVA_AZ 54-2531.01-47_06) and the Ethical Committee on Animal Experiments of the Radboud University, Nijmegen (RU-DEC 2011-124, 2011-230, 2013-008, 2013-125), in accordance with both the German and Dutch Animal Experimentation Acts and the Federation of European Laboratory Animal Science Associations protocol (http://

www.felasa.eu/guidelines.php) or performed according to the institutional guidelines for animal care and handling of the Institutional Animal Care and Use Committee of The University of Texas MD Anderson Cancer Center (ACUF 07-11-07631 and -07632).

Skin window model, intravital microscopy, and image analysis

Dorsal skin imaging windows were transplanted onto 10–14-wk-old male athymic Balb/c nude mice (CANN.CG-FOXN1NU/CRL; Charles River), as described (Alexander et al., 2008). 1 d after surgery, tumor cells ($\sim 5 \times 10^5$ cells in 4 µl PBS) were implanted into the dermis by image-guided microinjection. Tumor progression and therapy response were typically monitored for ≤14 d using a titanium window. In selected experiments, monitoring for 26 d was achieved using a polyethylene window. Tumors used for histological analysis of the DDR were harvested 4 or 5 d after implantation, representing the time point of radiation therapy initiation. Dual-vector control xenografts showed no significant differences in growth and invasion parameters compared with wild-type tumors and thus were used interchangeably as controls. For intravital microscopy, live mice were anesthetized with isofluorane and stably mounted onto a temperature-controlled platform (37°C). Progression of dual-color tumors was monitored using longitudinal multiphoton microscopy (LaVision BioTech; Andresen et al., 2009; Weigelin et al., 2015). By taking overview images of the entire tumor and surrounding vascular network before subcellular multiphoton microscopy, regions of interest for detailed image acquisition could be repetitively annotated and traced over multiple days and measurements. The emission ranges (in nm) were 400/40 (blue), 535/50 (green), 605/70 (red), and 710/75 (far-red). Epifluorescence overviews of xenografts were obtained with a 4× objective (numerical aperture [NA] 0.3) and subcellular-resolved multiphoton microscopy with a 20× objective (NA 0.95; both Olympus). Sequential 3D stacks were obtained for ≤300-µm penetration depth at 5-µm step intervals. Perfused blood vessels were visualized by i.v. injection of Alexa Fluor 660–conjugated dextran (70 kD, 1 mg/mouse; Invitrogen).

Images obtained during intravital microscopy were 3D reconstructed, stitched, and analyzed using ImageJ v1.40g (National Institutes of Health), ImSpector 3.4 (LaVision BioTec), Photoshop CS 8.0.1 (Adobe Systems), and Volocity 4.0.1 (Improvision). Unless indicated otherwise, multiphoton micrographs represent z-projections of 120–250-µm imaging depth. Migration velocities were obtained by computer-assisted cell tracking of invasion strand tips (Autocell software, Universities of Bremen and Würzburg). Tumor volume from epifluorescence overview images was calculated as $[((tumor\ width)^2 \times (tumor\ length) \times \pi) / 6] / 2$, to account for partial flattening of the tumor caused by the geometric constraints caused by the imaging window (compare Fig. S1 G, core). Fractions of mitotic and dead cells were determined from the morphology of tumor cell nuclei identified by H2B-EGFP from 5–30 multiple visual fields (dependent on analyzable cell amounts) from three to five independent tumors. The orientation of mitotic planes was expressed as angle relative to the length axis of the invasion strand, measured in invading cells and the adjacent core of the

lesion. The classification of invasion mode of surviving cells after IR was done based on the cytoplasmic DsRed2 marker: cells were counted as collective when cytosols appeared connected. This resulted in a sensitivity of 67% to detect collectively invading cells and 100% detection rate for individual cells. The extent of the residual tumor mass after treatments was measured as the area covered by the tumor core or invading cells at day 13 normalized to the matching area of the same lesion at day 6 using stitched high-resolution overviews from 3D projections obtained by multiphoton microscopy.

Long-term monitoring of intradermal tumors

Intradermal xenograft lesions without imaging window were injected along the dorsal midline ($\sim 10^4$ cells in 20 µl PBS, 30G needle, two tumors per mouse) sparing rostral and caudal zones. Correct intradermal positioning of growing tumors was verified by high-frequency ultrasound (DermaScan, Cortex Technology). Tumor development and therapy response were monitored by whole-body fluorescence imaging (FluorVivo100, INDEC BioSystems) and caliper measurements of macroscopic nodules (tumor volume = $[(tumor\ width)^2 \times (tumor\ length) \times \pi]/6$). Treatment of tumors was initiated at day 6 (HT-1080) or day 13 (MV3; Fig. 7 A), to secure a macroscopically visible tumor stage and equal size distribution between different groups. Inclusion criteria for treatment were at least one macroscopic, fluorescence-positive, and exponentially growing tumor lesion per mouse not exceeding a volume of 35 mm³ (HT-1080) or 40 mm³ (MV3). Before and during therapy, tumor development was monitored every second day. After therapy was completed, monitoring frequency was adjusted to the progression rate ranging from three times a week (growing tumor) to two times a month (complete regression) for up to 180 d. Humane endpoint criteria were a tumor size of 2 cm³, ulceration, weight loss, or poor overall condition due to internal metastasis. Sacrificed animals were screened for the presence of tumor remnants in the dorsal dermis, lymph nodes (superficial cervical, brachial, inguinal), lung, liver, and brain using fluorescence stereomicroscopy (Leica MZFLIII, NA 0.125, EL6000 external light source, GFP Plus and DsRed filter sets). This fluorescence-based approach to score organs for metastasis reliably detected micro- and macrometastasis events, but not individual cells. Tumor material and organs were embedded in optimal cutting temperature compound (O.C.T.; Sakura), deeply frozen using dry ice or through swaying in liquid nitrogen, stored at –80°C, and analyzed for the presence or absence of tumor cells or invasion status from 10–50-µm-thick cryosections (M500 or HM500OM Cryostat Microtome; Microm) by epifluorescence microscopy (Leica DMRA fluorescence microscope, Leica DFC340 FX charge-coupled device camera, Cytofluor software; 2.5× to 40× objectives, NA 0.07, 0.15, 0.3, 0.5, 0.75). A fixed monolayer of HT-1080 or MV3 dual-color cells from in vitro culture served as positive control to discriminate specific fluorescence from autofluorescence.

Antibody treatment

Adhesion-perturbing mouse anti-human β1 (clone 4B4, IgG1, 1 mg/ml; 6603113; Beckman Coulter) and αV integrin (clone 17E6,

batch 7299DA01.G01 and CH009, IgG1, 1 mg/ml, endotoxin level 0.4 EU/ml antibody; Merck Serono; kindly provided by Simon Goodman, Department of Cellular Pharmacology Oncology Platform, Merck, Darmstadt, Germany) mAb or mouse IgG1κ isotype (clone MOPC-21, M7894, 1 mg/ml; Sigma-Aldrich) were injected i.p. at 5 or 10 mg/kg body weight, respectively, to reach a calculated antibody concentration of ∼8 µg/ml in body fluids (60% of body weight; Chapman et al., 2010) which ranges more than two times above the minimum concentration required for 99% integrin epitope saturation in vitro (Fig. S4 F and data not shown). Based on an IgG1 half-life of 6–8 d (Vieira and Rajewsky, 1988), a calculated antibody concentration of >3 µg/ml in body fluids is achieved for ≥6 d by a single injection, sufficient to achieve >99% epitope saturation on HT1080 cells (Fig. S4 F). To additionally secure sufficient availability during the therapy phase, antibody was administered every 2–3 d starting with a boost (two injections on two subsequent days). Both mAbs 4B4 and 17E6 recognize human-specific epitopes and do not cross-react with murine integrins (Mahalingam et al., 2014; Takada and Puzon, 1993), allowing selective targeting of integrins expressed by tumor compartment but not the murine stroma. For application in vivo, NaN₃-containing antibody stocks (mAb 4B4, IgG1) were dialyzed against 0.9% NaCl using a dialysis tube with 14-kD exclusion limit (Roth). In mice carrying the imaging window, antibody was administered at days 3, 4, 7, 10, and 13 as a therapeutic intervention in established tumors after the onset of invasion (Fig. 6 A). Mice carrying established tumors without an imaging window received antibody on days 6 (before IR), 7, 9, 11, and 13 (HT-1080) or days 13 (before IR), 14, 16, 18, and 20 (MV3) after tumor implantation (Fig. 7 A).

IR procedures

Tumors in mice carrying the imaging window were irradiated either locally with a focused beam of 2-cm diameter using a RT 50 (x-ray) source (Philips Medical Systems) at a dose rate of 4.9 Gy/min or with a wide-field beam using an x-ray tube (X-RAD 320ix, Precision X-Ray) with 0.75-mm tin, 0.25-mm copper, and 1.5-mm aluminum filter for beam conditioning, 30-cm source-skin distance, 320-KV output voltage with 12.5 mA, for a dose rate of 3.6 Gy/min. To shield the mouse body but expose the tumor and peritumor tissue to the wide-field radiation beam, the mouse was placed inside a 6-mm lead-coated tube, while the tumor in the skin-fold window was exposed through a slit. To irradiate tumors in imaging window–free mice using the nonfocused beam, the mouse was positioned inside the shielding tube and the skin fold containing the tumor was gently extended through the slit, fixed by surgical tape and exposed to the radiation field. By varying the duration of exposure, radiation doses ranging from 2 to 10 Gy per session were applied. For tumors growing in the imaging window, a fractionation scheme with cumulative doses of 40 Gy for HT-1080 tumors (daily fractionation from days 4 to 8) or 50 Gy for MV3 tumors (days 4, 5, 7, 8, and 11) was used (Fig. 2 A), to reach detectable response curves within a 2-wk period for intravital microscopy. Tumors used for the analysis of DNA damage markers received a single dose of either 8 Gy (HT-1080) or 10 Gy (MV3) on day 4. Intradermal tumors in imaging window–free mice used for long-term

follow-up obtained a fractionated scheme with adjusted individual doses of 2 Gy from days 6 to 10 (HT-1080) or 3 Gy on days 13, 14, 16, 17, and 20 (MV3) after tumor implantation, amounting to cumulative 10 Gy (HT-1080) or 15 Gy (MV3; Fig. 7 A). This middose scheme was established by dose escalation and long-term monitoring to yield relapse frequencies of 60–80%, corresponding to ∼30% cure rate, for detecting the long-term effects of radiosensitization by integrin-targeted combination therapy (Fig. S5 G).

Immunohistological stainings

For the visualization of cell–cell junctions via ALCAM staining, untreated tumor-bearing mice carrying the skin window were sacrificed on day 5 (HT-1080) or day 8 (MV3) after tumor implantation. Tumor-containing dorsal skin samples were cryopreserved as described above, with marked orientation of invasion strands and invasion status documented by intravital epifluorescence microscopy. Frozen tissue samples were cut into 50-µm-thick cryosections (HM500OM Cryostat Microtome, Microm) that were immediately incubated in neutral buffered formalin (4%, formulation according to Lillie; ∼18 h, room temperature [RT]) and stored in phosphate buffer (0.1 M, pH 7.4, 4°C). For staining, free aldehyde groups and unspecific epitopes were blocked using 0.15% glycine in Tris-buffered saline (TBS; 30 min, RT), followed by incubation with TBS supplemented with 1% BSA (Sigma-Aldrich) and 15% normal goat serum (NGS; 30–60 min, RT; Gibco Life Technologies). After washing (TBS), endogenous mouse IgG in the tissue was blocked with unlabeled anti-mouse IgG Fab′ fragments (115-007-003, ∼18 h, 4°C; Jackson ImmunoResearch) followed by washing (TBS). Mouse anti-ALCAM mAb (AZN-L50; IgG2A; kindly provided by Joost te Riet, Department of Tumor Immunology, Radboudumc, Nijmegen, Netherlands; Nelissen et al., 2000) was biotinylated using biotin-SP (long-spacer) conjugated anti-mouse IgG Fab fragment (115-067-003, 1:2, 20 min, RT; Jackson ImmunoResearch), followed by incubation in mouse serum (10 µl/1 µg Fab′ biotin, 10 min, RT; Biowest). Anti-ALCAM/biotin-Fab′ complexes were diluted (1:15) in TBS/BSA (1%) and added to the tissue slices for incubation (∼18 h, 4°C). After washing (TBS), tissue slices were overlaid with streptavidin-coupled Alexa Fluor 647 (016-600-084, 2 µg/ml; Jackson ImmunoResearch) and DAPI (1 µg/ml; Roche), in TBS/BSA (1%, 20 min, RT), washed (TBS), and mounted in Fluoromount G (Southern Biotech) on object slides for confocal microscopy.

For analysis of DDR markers, nonirradiated or irradiated tumors (day 4 or 5) grown in the imaging window were obtained before or 30–60 min and 23–24 h after IR. Tumor-containing skin samples were cryopreserved with marked invasion status as described above. Frozen tissue samples were cut into 10-µm cryosections (HM500 Cryostat Microtome, Microm), mounted on Superfrost-plus object slides and screened to determine tumor subregion as core or invasion zone. After drying for ∼18 h, tissue slices were stored (–80°C) and, before staining, fixed (2% paraformaldehyde diluted in PHEM buffer [Pipes, Hepes, EGTA, and MgCl₂], 15 min, RT), rinsed with PBS, and incubated in PBS containing 0.1% Triton X-100 (Sigma-Aldrich) for permeabilization (20 min, RT). To minimize background, samples

were incubated in PBS supplemented with 5% NGS and 0.1% coldwater fish skin gelatin (CWFG; 30 min, RT; Sigma-Aldrich), followed by staining with the following primary antibodies: rabbit anti-γH2AX (pSer139, NB-100-384, 1:10,000; stock concentration 1 mg/ml; Novus Biologicals), rabbit anti-phosphoChk2 (pThr68, ab85743, 1:1,000; stock concentration 0.6 mg/ml; Abcam), or rabbit anti-phospho(Ser/Thr)-ATM/ATR-substrates (4F7, 2909, 1:1,000; Cell Signaling), all diluted in PBS supplemented with 2% NGS and 0.1% CWFG. Tissue slices were incubated with primary antibody solution (1 h at RT followed by ~18 h at 4°C); washed (PBS); incubated with goat anti-rabbit IgG (heavy and light chain [H+L]) Alexa Fluor 647 (A-21245, 4 µg/ml; Invitrogen) and DAPI (1 µg/ml), both diluted in PBS/NGS (2%)/CWFG (0.1%); washed; and mounted in Fluoromount G. For reliable intratumor comparison of subregions, all slices per tumor sample and staining were processed and recorded in parallel.

Hypoxia and phospho-p44/42-MAPK signals were detected in tumors 7 d after implantation from window-bearing mice. As a hypoxia probe, pimonidazole (Hypoxyprobe-1 Kit, Hypoxyprobe) was applied i.p. (60 mg/kg body weight), and tissue was harvested 60 min thereafter. Tumor-containing samples were cryopreserved with marked invasion status and processed as 10-µm-thick cryosections. Fixation, staining, and mounting were performed as described for immunohistological analysis of DDR markers using primary rat anti-CD31 (clone MEC13.3, 1:100, blood vessel staining; BD Biosciences), mouse anti-pimonidazole adducts (Hypoxyprobe-1 Kit, staining hypoxic cells), and rabbit anti-phospho-p44/42-MAPK antibody (Thr202/Tyr204, 9101, 1:50, phospho-Erk1/2 signal; Cell Signaling) and secondary goat anti-rat, anti-rabbit, or anti-mouse IgG (H+L) Alexa Fluor 488 or 647 (Invitrogen) antibodies.

3D in vitro collagen cultures of irradiated MV3 tumoroids were prepared and fixed as described (Veelken et al., 2017). Immunostaining was performed using rabbit anti-cleaved caspase-3 antibody (clone 5A1E, 9664, 1:200; Cell Signaling Technology) and goat anti-rabbit Alexa Fluor 568 (1:400; Invitrogen; Veelken et al., 2017).

Image acquisition and analysis
Tissue samples stained for ALCAM and DDR markers were analyzed by confocal microscopy (Olympus FV1000) as 3D stacks. ALCAM stainings were recorded using either a 20×/0.50 NA water or 60×/1.35 NA oil immersion objective with 3- or 1-µm step size, respectively. Stainings of DDR markers were scanned with a 40×/0.80 NA water immersion objective and 3-µm step size to represent the whole 10-µm tissue slice using identical instrument settings for each tumor sample and staining. Hypoxia and phosphoErk staining were scanned as z-stacks (2-µm step depth) on an LSM 510 META confocal microscope (Zeiss).

Using Fiji/ImageJ software (v1.48; Schindelin et al., 2012), DDR staining in tumor subregions was analyzed from average-intensity projections of ~10-µm 3D stacks, followed by image segmentation using the H2B-EGFP signal to identify and mark the edges of tumor nuclei (Fig. S3 C). Compared with maximum-intensity projections, the average-intensity projection resulted in cleaner image segmentation with fewer regions of interest

≤1 µm² incurred from irrelevant particles and background noise signal (data not shown). The mean gray value representing an individual DDR signal was quantified for large nuclear segments (≥38 µm²) representing intact, nonapoptotic nuclei, and the values were corrected for the background signal measured in nonnuclear regions (Fig. S3, C and D). Because image acquisition was optimized to identify intratumor heterogeneity, direct comparison of data points from different time points was obsolete.

Immunohistochemistry
Human tissue was fixed in 4% PBS-buffered formalin, routinely processed, and paraffin embedded. Mouse dorsal skin was cryopreserved as described above. 2–4-µm-thick sections of human tissue and 10-µm-thick sections of mouse tissue were stained with H&E and subsequently immunohistochemically stained by HRP reaction using mouse monoclonal anti-human α-smooth muscle actin (clone 1A4, DAKO, 1:500) or in-house-generated rabbit polyclonal anti-GFP (Department of Cell Biology, Radboudumc, Nijmegen, Netherlands; Cuppen, 1999) after antigen retrieval. Slide scanning was performed on a Leica DM6000B microscope (2.5× to 40× objectives, NA 0.07, 0.15, 0.3, 0.5, 0.75).

Protein gel electrophoresis and Western blot
β1 integrin knockdown efficiency in HT-1080 cells was detected by protein gel electrophoresis and Western blot analysis using whole-cell lysates. β1 integrin was detected with mouse anti-β1 integrin (clone 18/CD29, 0.25 µg/ml; BD Biosciences) and α-tubulin, as loading control with mouse anti-α-tubulin (clone DM1A; 1 µg/ml; Millipore). All protein samples were separated under reducing conditions on 8% SDS-PAGE and transferred onto a nitrocellulose membrane, blocked with 2% milk–PBS-Tween (1 h, RT), incubated with primary antibody (~18 h, 4°C), washed with PBS-Tween, and incubated with HRP-conjugated anti-mouse antibody (1 h, RT; Jackson ImmunoResearch). Protein bands were detected using luminol/H$_2$O$_2$. To detect multiple proteins on the same membrane, membranes were stripped using Restore Western Blot Stripping buffer (Thermo Fisher Scientific), blocked again, and labeled with subsequent primary and secondary antibody.

Flow cytometry
The surface expression of adhesion molecules on HT-1080 wild-type, vector control (p-puro or p-puro/p-neo), and stable knockdown (β1RNAi or β1/β3RNAi) cells and wild-type MV3 melanoma cells were obtained using cells from 3D matrix conditions after 24-h culture in 3D collagen lattices. Suspended cells were obtained by digestion with collagenase I (1,000 U/ml, 30 min, 37°C; Sigma-Aldrich), pelleted, and stained for 30 min on ice with the following monoclonal antibodies or isotypic control antibody: mouse anti-α1 integrin (clone TS2/7, 10 µg/ml; Abcam); mouse anti-α2 (CD49b, clone AK-7, 5 µg/ml), mouse anti-α3 integrin (CD49c, clone C3II.1, 0.25 µg/ml; both BD Biosciences); mouse anti-α5 integrin (clone SAM-1, 400 µg/ml; Millipore); rat anti-α6 integrin (CD49f, clone GoH3, 2.5 µg/ml; BD Biosciences); mouse anti-αV (CD51, clone AMF7, 50 mg/ml; Beckman Coulter); mouse anti-β1 (CD29, clone 4B4, 10 µg/ml),

mouse anti-β2 (CD18, clone 7E4, 10 µg/ml), mouse anti-β3 integrin (CD61, clone SZ21, 15 µg/ml; all Beckman Coulter); rat anti-β4 (CD104, clone 439-9B, 0.625 µg/ml; BD Biosciences); mouse anti-β5 integrin (clone EM09902, 2 µg/ml; Absolute Antibody); mouse anti-β6 (clone 437211, 0.5 µg/ml; R&D Systems); rat anti-β7 integrin (clone FIB504, 0.3125 µg/ml; BD Biosciences); mouse anti-β8 integrin (clone 416922, 10 µg/ml; R&D Systems); and isotypic mouse IgG1κ (clone MOPC-21) and IgG2bκ (clone 27-35), rat IgG2aκ (clone R35-95), and IgG2bκ (clone A95-1; all BD Biosciences). Integrin α4 was not included in the panel, as its expression has been shown to be restricted to leukocytes. When primary antibody was unconjugated, secondary mouse IgG (H+L) antibodies conjugated to Alexa Fluor 488 (20 µg/ml; Invitrogen) were used for detection. Viability of cells was obtained using propidium iodide (1 µg/ml) exclusion.

For measurement of residual β1 integrin epitopes after shRNA-mediated downregulation, cells were preincubated (45 min, 4°C) with unconjugated anti-β1 mAb 4B4 or isotypic IgG1κ (10 µg/ml), washed (PBS, 4°C), and incubated with FITC-conjugated mAb4B4 (10 µg/ml, 45 min, 4°C) to detect available β1 integrin epitopes.

Statistical analysis

For comparative analysis of DDR markers in tumor subregions, data were log transformed, and a longitudinal analysis in the form of a mixed-model ANOVA was performed using the lmer function of the R package lme4 (Bates et al., 2015). Per DDR marker and time point (before/after IR), differences between the variables "tumor sample" and "subregion" (i.e., core versus invasion zone) were analyzed. Due to the high number of data points and high intertumor variability, each comparison between tumor subregions resulted in statistically significant differences, even when independent replicates of the same condition were compared based on quantitatively minor sample-to-sample variation with typically inconsistent trends (Fig. S3 G, left panel). To separate biologically relevant effects from background variability, comparisons showing inconsistent data trends were considered nonsignificant, whereas analyses with consistent trends (i.e., similar slope and direction of mean of log values between tumor subregions; Fig. S3 G, right panel) were considered biologically significant, with P values displayed. Survival of tumor-bearing mice during long-term follow-up was analyzed using the Mantel–Cox log-rank test. For all other statistical analyses, Student's t test was used for paired samples with Gaussian distribution. For independent samples, irrespective of distribution, the two-tailed Mann–Whitney U test was used. For all multiple analyses, Bonferroni correction was performed. Unless mentioned otherwise, GraphPad Prism 5 or 6 software was used for statistical analysis.

Online supplemental material

Fig. S1 shows kinetics and organization of collective invasion in mouse dermis and comparison to human samples. Fig. S2 shows workflow and quantitative analysis of the radiation response of sarcoma and melanoma tumor subregions monitored by intravital microscopy. Fig. S3 shows tumor subregion analysis of the DDR by serial sectioning and image analysis. Fig. S4 shows integrin expression profiles in HT-1080 and MV3 cells and RNAi-based integrin targeting in HT-1080 cells. Fig. S5 shows radiosensitization of sarcoma and melanoma tumors by antibody-based integrin interference and procedures and outcome of long-term therapy response. Table S1 shows survival rates and tumor outcome for long-term follow up experiments on integrin-targeted and IR therapy in HT-1080 sarcoma xenografts. Table S2 shows survival rates and tumor outcome for long-term follow up experiments on integrin-targeted and IR therapy in MV3 melanoma xenografts. Video 1 shows collective invasion strands of a HT-1080 sarcoma xenograft. Video 2 shows collective invasion strands of a MV3 melanoma xenograft. Video 3 shows differential radiation response in tumor core and collective invasion niche in HT-1080 sarcoma xenografts detected by intravital microscopy.

References

Aceto, N., A. Bardia, D.T. Miyamoto, M.C. Donaldson, B.S. Wittner, J.A. Spencer, M. Yu, A. Pely, A. Engstrom, H. Zhu, et al. 2014. Circulating tumor cell clusters are oligoclonal precursors of breast cancer metastasis. *Cell.* 158:1110–1122. https://doi.org/10.1016/j.cell.2014.07.013

Ahmed, K.M., R.K. Pandita, D.K. Singh, C.R. Hunt, and T.K. Pandita. 2018. β1-integrin impacts Rad51 stability and DNA double-strand break repair by homologous recombination. *Mol. Cell. Biol.* 38:e00672–e17. https://doi.org/10.1128/MCB.00672-17

Ahmed, K.M., H. Zhang, and C.C. Park. 2013. NF-κB regulates radioresistance mediated by β1-integrin in three-dimensional culture of breast cancer cells. *Cancer Res.* 73:3737–3748. https://doi.org/10.1158/0008-5472.CAN-12-3537

Alexander, S., and P. Friedl. 2012. Cancer invasion and resistance: interconnected processes of disease progression and therapy failure. *Trends Mol. Med.* 18:13–26. https://doi.org/10.1016/j.molmed.2011.11.003

Alexander, S., G.E. Koehl, M. Hirschberg, E.K. Geissler, and P. Friedl. 2008. Dynamic imaging of cancer growth and invasion: a modified skin-fold chamber model. *Histochem. Cell Biol.* 130:1147–1154. https://doi.org/10.1007/s00418-008-0529-1

Andresen, V., S. Alexander, W.-M. Heupel, M. Hirschberg, R.M. Hoffman, and P. Friedl. 2009. Infrared multiphoton microscopy: subcellular-resolved deep tissue imaging. *Curr. Opin. Biotechnol.* 20:54–62. https://doi.org/10.1016/j.copbio.2009.02.008

Babel, L., M. Grunewald, R. Lehn, M. Langhans, and T. Meckel. 2017. Direct evidence for cell adhesion-mediated radioresistance (CAM-RR) on the level of individual integrin β1 clusters. *Sci. Rep.* 7:3393. https://doi.org/10.1038/s41598-017-03414-4

Bates, D., M. Mächler, B. Bolker, and S. Walker. 2015. Fitting Linear Mixed-Effects Models Using lme4. *J. Stat. Softw.* 67:1–48. https://doi.org/10.18637/jss.v067.i01

Burmeister, B.H., M.A. Henderson, J. Ainslie, R. Fisher, J. Di Iulio, B.M. Smithers, A. Hong, K. Shannon, R.A. Scolyer, S. Carruthers, et al. 2012. Adjuvant radiotherapy versus observation alone for patients at risk of lymph-node field relapse after therapeutic lymphadenectomy for melanoma: a randomised trial. *Lancet Oncol.* 13:589–597. https://doi.org/10.1016/S1470-2045(12)70138-9

Carbonell, W.S., M. DeLay, A. Jahangiri, C.C. Park, and M.K. Aghi. 2013. β1 integrin targeting potentiates antiangiogenic therapy and inhibits the growth of bevacizumab-resistant glioblastoma. *Cancer Res.* 73:3145–3154. https://doi.org/10.1158/0008-5472.CAN-13-0011

Carlson, P., A. Dasgupta, C.A. Grzelak, J. Kim, A. Barrett, I.M. Coleman, R.E. Shor, E.T. Goddard, J. Dai, E.M. Schweitzer, et al. 2019. Targeting the perivascular niche sensitizes disseminated tumour cells to chemotherapy. *Nat. Cell Biol.* 21:238–250. https://doi.org/10.1038/s41556-018-0267-0

Cerezo, A., M.C. Guadamillas, J.G. Goetz, S. Sánchez-Perales, E. Klein, R.K. Assoian, and M.A. del Pozo. 2009. The absence of caveolin-1 increases proliferation and anchorage- independent growth by a Rac-dependent, Erk-independent mechanism. *Mol. Cell. Biol.* 29:5046–5059. https://doi.org/10.1128/MCB.00315-09

Chapman, M.E., L. Hu, C.F. Plato, and D.E. Kohan. 2010. Bioimpedance spectroscopy for the estimation of body fluid volumes in mice. *Am. J. Physiol. Renal Physiol.* 299:F280–F283. https://doi.org/10.1152/ajprenal.00113.2010

Chen, N., C.-C. Chen, and L.F. Lau. 2000. Adhesion of human skin fibroblasts to Cyr61 is mediated through integrin α 6β 1 and cell surface heparan sulfate proteoglycans. *J. Biol. Chem.* 275:24953–24961. https://doi.org/10.1074/jbc.M003040200

Cheung, K.J., and A.J. Ewald. 2016. A collective route to metastasis: Seeding by tumor cell clusters. *Science.* 352:167–169. https://doi.org/10.1126/science.aaf6546

Cheung, K.J., V. Padmanaban, V. Silvestri, K. Schipper, J.D. Cohen, A.N. Fairchild, M.A. Gorin, J.E. Verdone, K.J. Pienta, J.S. Bader, and A.J. Ewald. 2016. Polyclonal breast cancer metastases arise from collective dissemination of keratin 14-expressing tumor cell clusters. *Proc. Natl. Acad. Sci. USA.* 113:E854–E863. https://doi.org/10.1073/pnas.1508541113

Ciccia, A., and S.J. Elledge. 2010. The DNA damage response: making it safe to play with knives. *Mol. Cell.* 40:179–204. https://doi.org/10.1016/j.molcel.2010.09.019

Clark, W.H. Jr., L. From, E.A. Bernardino, and M.C. Mihm. 1969. The histogenesis and biologic behavior of primary human malignant melanomas of the skin. *Cancer Res.* 29:705–727.

Cuppen, E. 1999. *Characterization of the molecular environment of the protein tyrosine phosphatase PTP-BL.* Dissertation. Radboud University Nijmegen, Nijmegen, Netherlands.

Dahlbäck, K., H.C. Wulf, and B. Dahlbäck. 1993. Vitronectin in mouse skin: immunohistochemical demonstration of its association with cutaneous amyloid. *J. Invest. Dermatol.* 100:166–170. https://doi.org/10.1111/1523-1747.ep12462792

Denais, C.M., R.M. Gilbert, P. Isermann, A.L. McGregor, M. te Lindert, B. Weigelin, P.M. Davidson, P. Friedl, K. Wolf, and J. Lammerding. 2016. Nuclear envelope rupture and repair during cancer cell migration. *Science.* 352:353–358. https://doi.org/10.1126/science.aad7297

Dickreuter, E., I. Eke, M. Krause, K. Borgmann, M.A. van Vugt, and N. Cordes. 2016. Targeting of β1 integrins impairs DNA repair for radiosensitization of head and neck cancer cells. *Oncogene.* 35:1353–1362. https://doi.org/10.1038/onc.2015.212

Domoto, T., I.V. Pyko, T. Furuta, K. Miyashita, M. Uehara, T. Shimasaki, M. Nakada, and T. Minamoto. 2016. Glycogen synthase kinase-3β is a pivotal mediator of cancer invasion and resistance to therapy. *Cancer Sci.* 107:1363–1372. https://doi.org/10.1111/cas.13028

Eke, I., and N. Cordes. 2015. Focal adhesion signaling and therapy resistance in cancer. *Semin. Cancer Biol.* 31:65–75. https://doi.org/10.1016/j.semcancer.2014.07.009

Eke, I., Y. Deuse, S. Hehlgans, K. Gurtner, M. Krause, A. Baumann, A. Shevchenko, V. Sandfort, and N. Cordes. 2012. β1Integrin/FAK/cortactin signaling is essential for human head and neck cancer resistance to radiotherapy. *J. Clin. Invest.* 122:1529–1540. https://doi.org/10.1172/JCI61350

Élez, E., I. Kocáková, T. Höhler, U.M. Martens, C. Bokemeyer, E. Van Cutsem, B. Melichar, M. Smakal, T. Csőszi, E. Topuzov, et al. 2015. Abituzumab combined with cetuximab plus irinotecan versus cetuximab plus irinotecan alone for patients with *KRAS* wild-type metastatic colorectal cancer: the randomised phase I/II POSEIDON trial. *Ann. Oncol.* 26: 132–140. https://doi.org/10.1093/annonc/mdu474

Espenel, S., A. Vallard, C. Rancoule, M.A. Garcia, J.B. Guy, C. Chargari, E. Deutsch, and N. Magné. 2017. Melanoma: Last call for radiotherapy. *Crit. Rev. Oncol. Hematol.* 110:13–19. https://doi.org/10.1016/j.critrevonc.2016.12.003

Eyden, B.P., C. Manson, S.S. Banerjee, I.S. Roberts, and M. Harris. 1998. Sclerosing epithelioid fibrosarcoma: a study of five cases emphasizing diagnostic criteria. *Histopathology.* 33:354–360. https://doi.org/10.1046/j.1365-2559.1998.00530.x

Fedorenko, I.V., E.V. Abel, J.M. Koomen, B. Fang, E.R. Wood, Y.A. Chen, K.J. Fisher, S. Iyengar, K.B. Dahlman, J.A. Wargo, et al. 2016. Fibronectin induction abrogates the BRAF inhibitor response of BRAF V600E/PTEN-null melanoma cells. *Oncogene.* 35:1225–1235. https://doi.org/10.1038/onc.2015.188

Formenti, S.C., and S. Demaria. 2013. Combining radiotherapy and cancer immunotherapy: a paradigm shift. *J. Natl. Cancer Inst.* 105:256–265. https://doi.org/10.1093/jnci/djs629

Friedl, P., J. Locker, E. Sahai, and J.E. Segall. 2012. Classifying collective cancer cell invasion. *Nat. Cell Biol.* 14:777–783. https://doi.org/10.1038/ncb2548

Gérard, C., and A. Goldbeter. 2014. The balance between cell cycle arrest and cell proliferation: control by the extracellular matrix and by contact inhibition. *Interface Focus.* 4:20130075. https://doi.org/10.1098/rsfs.2013.0075

Ghatak, S., S. Misra, R.A. Norris, R.A. Moreno-Rodriguez, S. Hoffman, R.A. Levine, V.C. Hascall, and R.R. Markwald. 2014. Periostin induces intracellular cross-talk between kinases and hyaluronan in atrioventricular valvulogenesis. *J. Biol. Chem.* 289:8545–8561. https://doi.org/10.1074/jbc.M113.539882

Gibert, B., and P. Mehlen. 2015. Dependence Receptors and Cancer: Addiction to Trophic Ligands. *Cancer Res.* 75:5171–5175. https://doi.org/10.1158/0008-5472.CAN-14-3652

Giese, A., M.A. Loo, N. Tran, D. Haskett, S.W. Coons, and M.E. Berens. 1996. Dichotomy of astrocytoma migration and proliferation. *Int. J. Cancer.* 67: 275–282. https://doi.org/10.1002/(SICI)1097-0215(19960717)67:2<275::AID-IJC20>3.0.CO;2-9

Gorayski, P., B. Burmeister, and M. Foote. 2015. Radiotherapy for cutaneous melanoma: current and future applications. *Future Oncol.* 11:525–534. https://doi.org/10.2217/fon.14.300

Guadagnolo, B.A., V. Prieto, R. Weber, M.I. Ross, and G.K. Zagars. 2014. The role of adjuvant radiotherapy in the local management of desmoplastic melanoma. *Cancer.* 120:1361–1368. https://doi.org/10.1002/cncr.28415

Guo, W., and F.G. Giancotti. 2004. Integrin signalling during tumour progression. *Nat. Rev. Mol. Cell Biol.* 5:816–826. https://doi.org/10.1038/nrm1490

Haas, R.L., A. Gronchi, M.A.J. van de Sande, E.H. Baldini, H. Gelderblom, C. Messiou, E. Wardelmann, and A. Le Cesne. 2018. Perioperative

Management of Extremity Soft Tissue Sarcomas. *J. Clin. Oncol.* 36: 118–124. https://doi.org/10.1200/JCO.2017.74.7527

Haas, R.L.M., H. Gelderblom, S. Sleijfer, H.H. van Boven, A. Scholten, L. Dewit, G. Borst, J. van der Hage, J.M. Kerst, R.A. Nout, et al. 2015. A phase I study on the combination of neoadjuvant radiotherapy plus pazopanib in patients with locally advanced soft tissue sarcoma of the extremities. *Acta Oncol.* 54:1195–1201. https://doi.org/10.3109/0284186X.2015.1037404

Hegerfeldt, Y., M. Tusch, E.B. Bröcker, and P. Friedl. 2002. Collective cell movement in primary melanoma explants: plasticity of cell-cell interaction, beta1-integrin function, and migration strategies. *Cancer Res.* 62: 2125–2130.

Hirata, E., M.R. Girotti, A. Viros, S. Hooper, B. Spencer-Dene, M. Matsuda, J. Larkin, R. Marais, and E. Sahai. 2015. Intravital imaging reveals how BRAF inhibition generates drug-tolerant microenvironments with high integrin β1/FAK signaling. *Cancer Cell.* 27:574–588. https://doi.org/10.1016/j.ccell.2015.03.008

Hodivala-Dilke, K.M., K.P. McHugh, D.A. Tsakiris, H. Rayburn, D. Crowley, M. Ullman-Culleré, F.P. Ross, B.S. Coller, S. Teitelbaum, and R.O. Hynes. 1999. Beta3-integrin-deficient mice are a model for Glanzmann thrombasthenia showing placental defects and reduced survival. *J. Clin. Invest.* 103:229–238. https://doi.org/10.1172/JCI5487

Hodkinson, P.S., T. Elliott, W.S. Wong, R.C. Rintoul, A.C. Mackinnon, C. Haslett, and T. Sethi. 2006. ECM overrides DNA damage-induced cell cycle arrest and apoptosis in small-cell lung cancer cells through beta1 integrin-dependent activation of PI3-kinase. *Cell Death Differ.* 13: 1776–1788. https://doi.org/10.1038/sj.cdd.4401849

Hoefkens, F., C. Dehandschutter, J. Somville, P. Meijnders, and D. Van Gestel. 2016. Soft tissue sarcoma of the extremities: pending questions on surgery and radiotherapy. *Radiat. Oncol.* 11:136. https://doi.org/10.1186/s13014-016-0668-9

Houben, R., S. Hesbacher, C.P. Schmid, C.S. Kauczok, U. Flohr, S. Haferkamp, C.S.L. Müller, D. Schrama, J. Wischhusen, and J.C. Becker. 2011. High-level expression of wild-type p53 in melanoma cells is frequently associated with inactivity in p53 reporter gene assays. *PLoS One.* 6:e22096. https://doi.org/10.1371/journal.pone.0022096

Hsu, T.C., W.C. Dewey, and R.M. Humphrey. 1962. Radiosensitivity of cells of Chinese hamster in vitro in relation to the cell cycle. *Exp. Cell Res.* 27: 441–452. https://doi.org/10.1016/0014-4827(62)90010-1

Janes, S.M., and F.M. Watt. 2004. Switch from alphavbeta5 to alphavbeta6 integrin expression protects squamous cell carcinomas from anoikis. *J. Cell Biol.* 166:419–431. https://doi.org/10.1083/jcb.200312074

Jatana, K.R., P. Balasubramanian, K.P. McMullen, J.C. Lang, T.N. Teknos, and J.J. Chalmers. 2016. Effect of surgical intervention on circulating tumor cells in patients with squamous cell carcinoma of the head and neck using a negative enrichment technology. *Head Neck.* 38:1799–1803. https://doi.org/10.1002/hed.24519

Kanda, R., A. Kawahara, K. Watari, Y. Murakami, K. Sonoda, M. Maeda, H. Fujita, M. Kage, H. Uramoto, C. Costa, et al. 2013. Erlotinib resistance in lung cancer cells mediated by integrin β1/Src/Akt-driven bypass signaling. *Cancer Res.* 73:6243–6253. https://doi.org/10.1158/0008-5472.CAN-12-4502

Kim, M.Y., W.D. Cho, K.P. Hong, B. Choi, J.W. Hong, S. Kim, Y.R. Moon, S.M. Son, O.J. Lee, H.C. Lee, and H.G. Song. 2016. Novel monoclonal antibody against beta 1 integrin enhances cisplatin efficacy in human lung adenocarcinoma cells. *J. Biomed. Res.* 30:217–224. https://doi.org/10.7555/JBR.30.2016K0005

Kissler, S., P. Stern, K. Takahashi, K. Hunter, L.B. Peterson, and L.S. Wicker. 2006. In vivo RNA interference demonstrates a role for Nramp1 in modifying susceptibility to type 1 diabetes. *Nat. Genet.* 38:479–483. https://doi.org/10.1038/ng1766

Koivisto, L., J. Heino, L. Häkkinen, and H. Larjava. 2014. Integrins in Wound Healing. *Adv. Wound Care (New Rochelle).* 3:762–783. https://doi.org/10.1089/wound.2013.0436

Kris, M.G., L.E. Gaspar, J.E. Chaft, E.B. Kennedy, C.G. Azzoli, P.M. Ellis, S.H. Lin, H.I. Pass, R. Seth, F.A. Shepherd, et al. 2017. Adjuvant Systemic Therapy and Adjuvant Radiation Therapy for Stage I to IIIA Completely Resected Non-Small-Cell Lung Cancers: American Society of Clinical Oncology/Cancer Care Ontario Clinical Practice Guideline Update. *J. Clin. Oncol.* 35:2960–2974. https://doi.org/10.1200/JCO.2017.72.4401

Leith, J.T., A. Hercbergs, S. Kenney, S.A. Mousa, and P.J. Davis. 2018. Activation of tumor cell integrin αvβ3 by radiation and reversal of activation by chemically modified tetraiodothyroacetic acid (tetrac). *Endocr. Res.* 43:215–219. https://doi.org/10.1080/07435800.2018.1456550

Lu, X., D. Lu, M. Scully, and V. Kakkar. 2008. The role of integrins in cancer and the development of anti-integrin therapeutic agents for cancer therapy. *Perspect. Medicin. Chem.* 2:57–73. https://doi.org/10.1177/1177391X0800200003

Mahadevan, A., V.L. Patel, and N. Dagoglu. 2015. Radiation Therapy in the Management of Malignant Melanoma. *Oncology (Williston Park).* 29: 743–751.

Mahalingam, B., J.F. Van Agthoven, J.-P. Xiong, J.L. Alonso, B.D. Adair, X. Rui, S. Anand, M. Mehrbod, M.R.K. Mofrad, C. Burger, et al. 2014. Atomic basis for the species-specific inhibition of αV integrins by monoclonal antibody 17E6 is revealed by the crystal structure of αVβ3 ectodomain-17E6 Fab complex. *J. Biol. Chem.* 289:13801–13809. https://doi.org/10.1074/jbc.M113.546929

Martinez-Outschoorn, U.E., R.M. Balliet, D.B. Rivadeneira, B. Chiavarina, S. Pavlides, C. Wang, D. Whitaker-Menezes, K.M. Daumer, Z. Lin, A.K. Witkiewicz, et al. 2010. Oxidative stress in cancer associated fibroblasts drives tumor-stroma co-evolution: A new paradigm for understanding tumor metabolism, the field effect and genomic instability in cancer cells. *Cell Cycle.* 9:3256–3276. https://doi.org/10.4161/cc.9.16.12553

Mauger, A., H. Emonard, D.J. Hartmann, J.M. Foidart, and P. Sengel. 1987. Immunofluorescent localization of collagen types I, III and IV, fibronectin, laminin, and basement membrane proteoglycan in developing mouse skin. *Rouxs Arch. Dev. Biol.* 196:295–302. https://doi.org/10.1007/BF00395953

McQuade, K.J., D.M. Beauvais, B.J. Burbach, and A.C. Rapraeger. 2006. Syndecan-1 regulates alphavbeta5 integrin activity in B82L fibroblasts. *J. Cell Sci.* 119:2445–2456. https://doi.org/10.1242/jcs.02970

Mikkelsen, T., C. Brodie, S. Finniss, M.E. Berens, J.L. Rennert, K. Nelson, N. Lemke, S.L. Brown, D. Hahn, B. Neuteboom, and S.L. Goodman. 2009. Radiation sensitization of glioblastoma by cilengitide has unanticipated schedule-dependency. *Int. J. Cancer.* 124:2719–2727. https://doi.org/10.1002/ijc.24240

Mitjans, F., D. Sander, J. Adán, A. Sutter, J.M. Martinez, C.S. Jäggle, J.M. Moyano, H.G. Kreysch, J. Piulats, and S.L. Goodman. 1995. An anti-alpha v-integrin antibody that blocks integrin function inhibits the development of a human melanoma in nude mice. *J. Cell Sci.* 108:2825–2838.

Monferran, S., N. Skuli, C. Delmas, G. Favre, J. Bonnet, E. Cohen-Jonathan-Moyal, and C. Toulas. 2008. Alphavbeta3 and alphavbeta5 integrins control glioma cell response to ionising radiation through ILK and RhoB. *Int. J. Cancer.* 123:357–364. https://doi.org/10.1002/ijc.23498

Naci, D., M.-A. El Azreq, N. Chetoui, L. Lauden, F. Sigaux, D. Charron, R. Al-Daccak, and F. Aoudjit. 2012. α2β1 integrin promotes chemoresistance against doxorubicin in cancer cells through extracellular signal-regulated kinase (ERK). *J. Biol. Chem.* 287:17065–17076. https://doi.org/10.1074/jbc.M112.349365

Naci, D., K. Vuori, and F. Aoudjit. 2015. Alpha2beta1 integrin in cancer development and chemoresistance. *Semin. Cancer Biol.* 35:145–153. https://doi.org/10.1016/j.semcancer.2015.08.004

Nelissen, J.M.D.T., I.M. Peters, B.G. de Grooth, Y. van Kooyk, and C.G. Figdor. 2000. Dynamic regulation of activated leukocyte cell adhesion molecule-mediated homotypic cell adhesion through the actin cytoskeleton. *Mol. Biol. Cell.* 11:2057–2068. https://doi.org/10.1091/mbc.11.6.2057

Nieto, M.A., R.Y.-J. Huang, R.A. Jackson, and J.P. Thiery. 2016. EMT: 2016. *Cell.* 166:21–45. https://doi.org/10.1016/j.cell.2016.06.028

Paoli, P., E. Giannoni, and P. Chiarugi. 2013. Anoikis molecular pathways and its role in cancer progression. *Biochim. Biophys. Acta.* 1833:3481–3498. https://doi.org/10.1016/j.bbamcr.2013.06.026

Park, C.C., H. Zhang, M. Pallavicini, J.W. Gray, F. Baehner, C.J. Park, and M.J. Bissell. 2006. β1 integrin inhibitory antibody induces apoptosis of breast cancer cells, inhibits growth, and distinguishes malignant from normal phenotype in three dimensional cultures and in vivo. *Cancer Res.* 66:1526–1535. https://doi.org/10.1158/0008-5472.CAN-05-3071

Park, C.C., H.J. Zhang, E.S. Yao, C.J. Park, and M.J. Bissell. 2008. Beta1 integrin inhibition dramatically enhances radiotherapy efficacy in human breast cancer xenografts. *Cancer Res.* 68:4398–4405. https://doi.org/10.1158/0008-5472.CAN-07-6390

Pickup, M.W., J.K. Mouw, and V.M. Weaver. 2014. The extracellular matrix modulates the hallmarks of cancer. *EMBO Rep.* 15:1243–1253. https://doi.org/10.15252/embr.201439246

Raab-Westphal, S., J.F. Marshall, and S.L. Goodman. 2017. Integrins as therapeutic targets: Successes and cancers. *Cancers (Basel).* 9:1–28. https://doi.org/10.3390/cancers9090110

Radisky, D.C., D.D. Levy, L.E. Littlepage, H. Liu, C.M. Nelson, J.E. Fata, D. Leake, E.L. Godden, D.G. Albertson, M.A. Nieto, et al. 2005. Rac1b and

reactive oxygen species mediate MMP-3-induced EMT and genomic instability. *Nature.* 436:123–127. https://doi.org/10.1038/nature03688

Rahbari, N.N., D. Kedrin, J. Incio, H. Liu, W.W. Ho, H.T. Nia, C.M. Edrich, K. Jung, J. Daubriac, I. Chen, et al. 2016. Anti-VEGF therapy induces ECM remodeling and mechanical barriers to therapy in colorectal cancer liver metastases. *Sci. Transl. Med.* 8:360ra135. https://doi.org/10.1126/scitranslmed.aaf5219

Rasheed, S., W.A. Nelson-Rees, E.M. Toth, P. Arnstein, and M.B. Gardner. 1974. Characterization of a newly derived human sarcoma cell line (HT-1080). *Cancer.* 33:1027–1033. https://doi.org/10.1002/1097-0142(197404)33:4<1027::AID-CNCR2820330419>3.0.CO;2-Z

Rogakou, E.P., D.R. Pilch, A.H. Orr, V.S. Ivanova, and W.M. Bonner. 1998. DNA double-stranded breaks induce histone H2AX phosphorylation on serine 139. *J. Biol. Chem.* 273:5858–5868. https://doi.org/10.1074/jbc.273.10.5858

Roth, W., C. Wild-Bode, M. Platten, C. Grimmel, H.S. Melkonyan, J. Dichgans, and M. Weller. 2000. Secreted Frizzled-related proteins inhibit motility and promote growth of human malignant glioma cells. *Oncogene.* 19:4210–4220. https://doi.org/10.1038/sj.onc.1203783

Schindelin, J., I. Arganda-Carreras, E. Frise, V. Kaynig, M. Longair, T. Pietzsch, S. Preibisch, C. Rueden, S. Saalfeld, B. Schmid, et al. 2012. Fiji: an open-source platform for biological-image analysis. *Nat. Methods.* 9:676–682. https://doi.org/10.1038/nmeth.2019

Seguin, L., J.S. Desgrosellier, S.M. Weis, and D.A. Cheresh. 2015. Integrins and cancer: regulators of cancer stemness, metastasis, and drug resistance. *Trends Cell Biol.* 25:234–240. https://doi.org/10.1016/j.tcb.2014.12.006

Seguin, L., S. Kato, A. Franovic, M.F. Camargo, J. Lesperance, K.C. Elliott, M. Yebra, A. Mielgo, A.M. Lowy, H. Husain, et al. 2014. An integrin β_3-KRAS-RalB complex drives tumour stemness and resistance to EGFR inhibition. *Nat. Cell Biol.* 16:457–468. https://doi.org/10.1038/ncb2953

Shiloh, Y., and Y. Ziv. 2013. The ATM protein kinase: regulating the cellular response to genotoxic stress, and more. *Nat. Rev. Mol. Cell Biol.* 14:197–210. https://doi.org/10.1038/nrm3546

Smerage, J.B., G.T. Budd, G.V. Doyle, M. Brown, C. Paoletti, M. Muniz, M.C. Miller, M.I. Repollet, D.A. Chianese, M.C. Connelly, et al. 2013. Monitoring apoptosis and Bcl-2 on circulating tumor cells in patients with metastatic breast cancer. *Mol. Oncol.* 7:680–692. https://doi.org/10.1016/j.molonc.2013.02.013

Takada, Y., and W. Puzon. 1993. Identification of a regulatory region of integrin beta 1 subunit using activating and inhibiting antibodies. *J. Biol. Chem.* 268:17597–17601.

Tarunina, M., and J.R. Jenkins. 1993. Human p53 binds DNA as a protein homodimer but monomeric variants retain full transcription transactivation activity. *Oncogene.* 8:3165–3173.

Tolaney, S.M., Y. Boucher, D.G. Duda, J.D. Martin, G. Seano, M. Ancukiewicz, W.T. Barry, S. Goel, J. Lahdenrata, S.J. Isakoff, et al. 2015. Role of vascular density and normalization in response to neoadjuvant bevacizumab and chemotherapy in breast cancer patients. *Proc. Natl. Acad. Sci. USA.* 112:14325–14330. https://doi.org/10.1073/pnas.1518808112

van Muijen, G.N., K.F. Jansen, I.M. Cornelissen, D.F. Smeets, J.L. Beck, and D.J. Ruiter. 1991. Establishment and characterization of a human melanoma cell line (MV3) which is highly metastatic in nude mice. *Int. J. Cancer.* 48:85–91. https://doi.org/10.1002/ijc.2910480116

Veelken, C., G.-J. Bakker, D. Drell, and P. Friedl. 2017. Single cell-based automated quantification of therapy responses of invasive cancer spheroids in organotypic 3D culture. *Methods.* 128:139–149. https://doi.org/10.1016/j.ymeth.2017.07.015

Vehlow, A., K. Storch, D. Matzke, and N. Cordes. 2016. Molecular Targeting of Integrins and Integrin-Associated Signaling Networks in Radiation Oncology. *Recent Results Cancer Res.* 198:89–106. https://doi.org/10.1007/978-3-662-49651-0_4

Verduzco, D., M. Lloyd, L. Xu, A. Ibrahim-Hashim, Y. Balagurunathan, R.A. Gatenby, and R.J. Gillies. 2015. Intermittent hypoxia selects for genotypes and phenotypes that increase survival, invasion, and therapy resistance. *PLoS One.* 10:e0120958. https://doi.org/10.1371/journal.pone.0120958

Vieira, P., and K. Rajewsky. 1988. The half-lives of serum immunoglobulins in adult mice. *Eur. J. Immunol.* 18:313–316. https://doi.org/10.1002/eji.1830180221

Weigelin, B., G.-J. Bakker, and P. Friedl. 2012. Intravital third harmonic generation microscopy of collective melanoma cell invasion: Principles of interface guidance and microvesicle dynamics. *Intravital.* 1:32–43. https://doi.org/10.4161/intv.21223

Weigelin, B., E. Bolaños, A. Teijeira, I. Martinez-Forero, S. Labiano, A. Azpilikueta, A. Morales-Kastresana, J.I. Quetglas, E. Wagena, A.R. Sánchez-Paulete, et al. 2015. Focusing and sustaining the antitumor CTL effector killer response by agonist anti-CD137 mAb. *Proc. Natl. Acad. Sci. USA.* 112:7551–7556. https://doi.org/10.1073/pnas.1506357112

Wellbrock, C., and I. Arozarena. 2016. The Complexity of the ERK/MAP-Kinase Pathway and the Treatment of Melanoma Skin Cancer. *Front. Cell Dev. Biol.* 4:33. https://doi.org/10.3389/fcell.2016.00033

Winograd-Katz, S.E., R. Fässler, B. Geiger, and K.R. Legate. 2014. The integrin adhesome: from genes and proteins to human disease. *Nat. Rev. Mol. Cell Biol.* 15:273–288. https://doi.org/10.1038/nrm3769

Yamaguchi, N., T. Mizutani, K. Kawabata, and H. Haga. 2015. Leader cells regulate collective cell migration via Rac activation in the downstream signaling of integrin β1 and PI3K. *Sci. Rep.* 5:7656. https://doi.org/10.1038/srep07656

Yamamoto, N., P. Jiang, M. Yang, M. Xu, K. Yamauchi, H. Tsuchiya, K. Tomita, G.M. Wahl, A.R. Moossa, and R.M. Hoffman. 2004. Cellular dynamics visualized in live cells in vitro and in vivo by differential dual-color nuclear-cytoplasmic fluorescent-protein expression. *Cancer Res.* 64:4251–4256. https://doi.org/10.1158/0008-5472.CAN-04-0643

Yu, X., S. Miyamoto, and E. Mekada. 2000. Integrin alpha 2 beta 1-dependent EGF receptor activation at cell-cell contact sites. *J. Cell Sci.* 113:2139–2147. https://doi.org/10.1083/jcb.109.4.1807

Zannini, L., D. Delia, and G. Buscemi. 2014. CHK2 kinase in the DNA damage response and beyond. *J. Mol. Cell Biol.* 6:442–457. https://doi.org/10.1093/jmcb/mju045
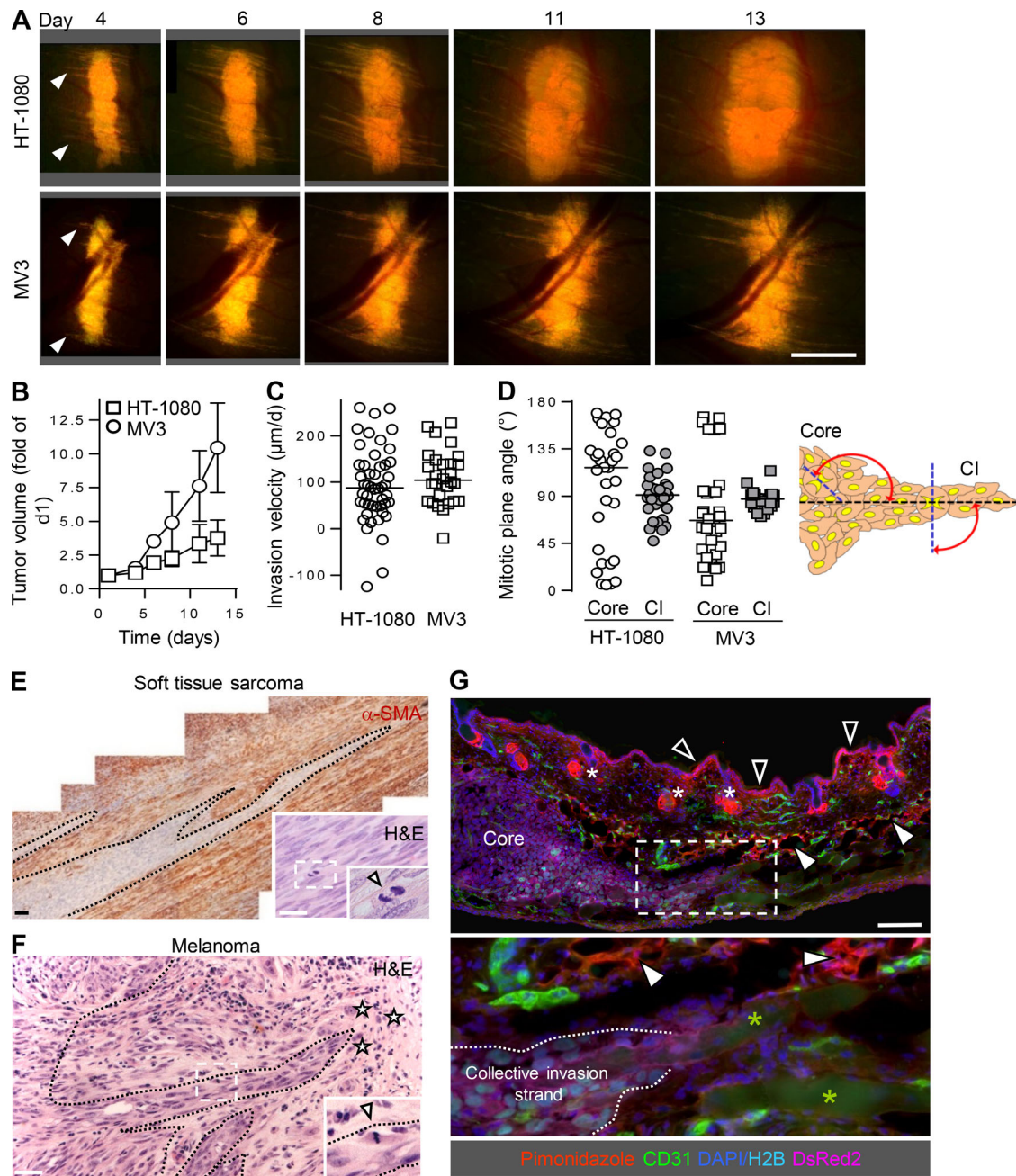
Supplemental material

Figure S1. **Kinetics and organization of collective invasion in mouse dermis and comparison to human samples. (A and B)** Time-dependent whole-tumor morphology (A) and tumor volume (B) of HT-1080 and MV3 xenografts in the skin window. Data represent the means and SD from five (HT-1080) and three (MV3) tumors. Arrowheads, onset of collective invasion. Scale bar, 1 mm. **(C)** Median velocity of collective invasion into the dermis. Data represent the distance migrated per day from day 4 to 6 of 48 (HT-1080) and 28 (MV3) individual collective strands from three (HT-1080) and two (MV3) tumors. Negative values originate from occasional rearward orientation or retraction of strand tips. **(D)** Orientation of mitotic planes in the core or collective invasion (CI) strands relative to the direction of migration. A median angle of ~90° reflects mitotic planes aligned perpendicular to the invasion direction. Per region and tumor type, ~30 mitotic planes were analyzed from one tumor. **(E)** Collective invasion pattern in human adult primary soft tissue sarcoma in subdiaphragmal location. Multicellular strands bordered by reactive α-smooth muscle actin (SMA)–positive stromal cells. Inset, mitotic planes (arrowhead) orientated perpendicularly to the invasion direction. Dashed lines, border between invasion zone and stroma. Scale bars, 100 µm. **(F)** Collective invasion pattern in human primary melanoma lesion during vertical growth phase with deep dermal invasion. Inset, mitotic plane (arrowhead) perpendicular to invasion direction. Dashed lines, border stroma to invasion zone. Asterisks, individual tumor cells. Scale bar, 100 µm. **(G)** Absence of hypoxic areas in HT-1080 xenograft after 7 d of growth in the skin window. Hypoxic regions detected by pimonidazole staining (red) include the upper epidermis (black arrowheads), sebaceous glands (white asterisks), and dermal fat tissue (white arrowheads), but not the tumor core. Green asterisks, autofluorescent myofibers. Scale bar, 1 mm.
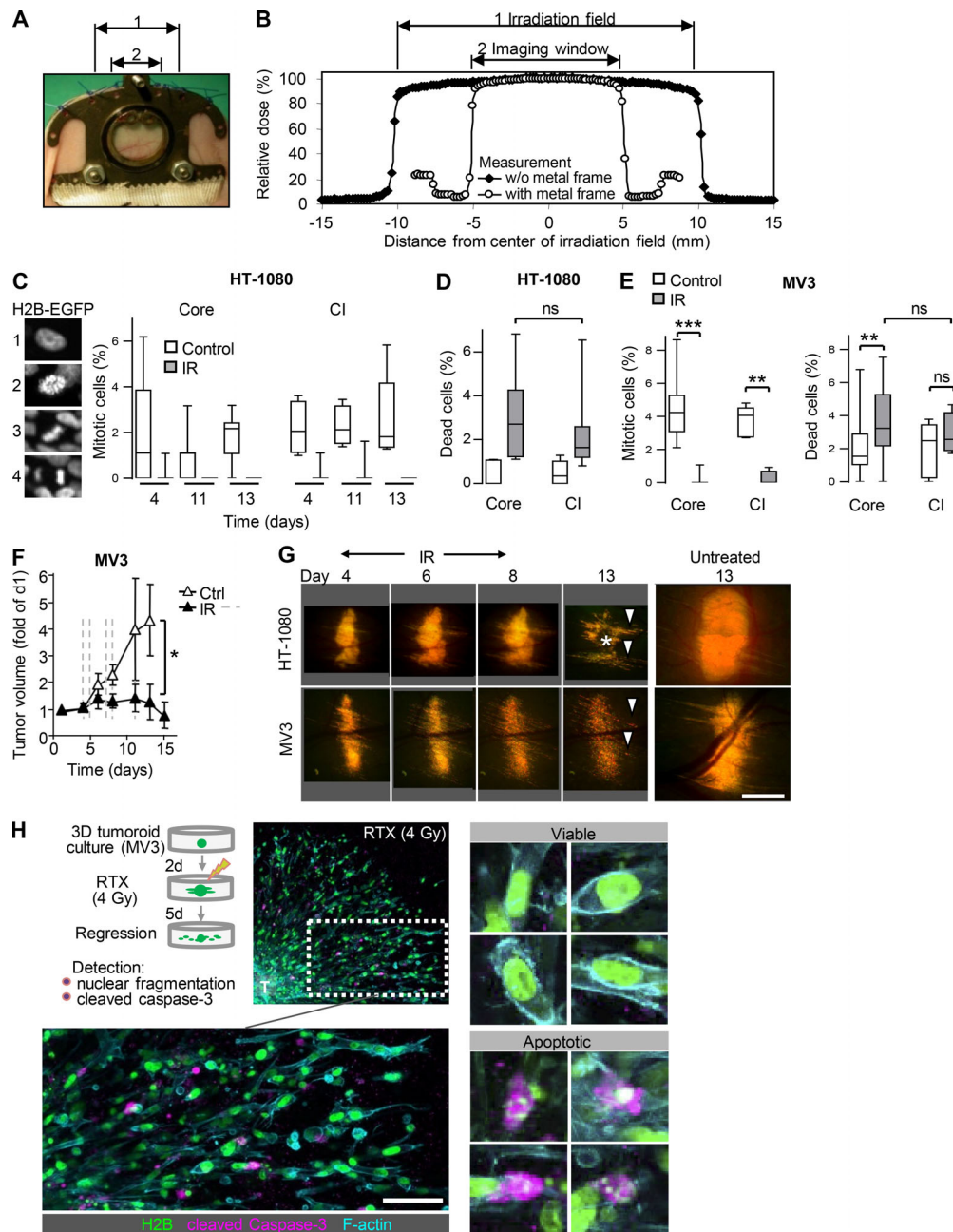
Figure S2. **Workflow and quantitative analysis of the radiation response of sarcoma and melanoma tumor subregions monitored by intravital microscopy. (A and B)** Dimensions and uniform dosing of IR across the visible field of the skin window using focal-beam IR (2-cm beam diameter). **(A)** Topography of the IR field (1) and skin window (2). **(B)** Dosimetry of IR measured across the IR field (1). Due to the metal frame of the imaging window, only the window itself (2) is exposed to IR. **(C)** Frequency of mitotic planes in HT-1080 tumor core and collective invasion strands, by scoring the H2B-EGFP pattern (1, interphase nucleus; 2–4, mitotic nuclei [2, prometaphase; 3, metaphase; 4, anaphase]). Data show the median fraction, 25th/75th percentiles (box), and 5th/95th percentiles (whiskers) from 5–20 different microscopic fields representing three to four tumors. Per tumor region and day, 10–20 nuclei were analyzed. **(D)** Frequency of dead cells in HT-1080 tumor cores and collective invasion strands (pooled data days 11 and 13). Data represent the medians, 25th/75th percentiles (box), and 5th/95th percentiles (whiskers) of ~80 nuclei per tumor region from 5–20 fields/tumor from three to four independent mice. Statistics, Mann–Whitney U test. **(E)** Frequency of mitotic and dead cells in tumor core or collective invasion (CI) zone of MV3 tumors (day 6). Data show the median fraction, 25th/75th percentiles (box), and 5th/95th percentiles (whiskers) of 10–20 nuclei per tumor region from 9–28 different microscopic fields representing four to five tumors. **, P = 0.004 (mitotic cells) or P = 0.002 (dead cells); ***, P < 0.0001; ns, not significant. Statistics, Mann–Whitney U test. **(F)** MV3 tumor growth before, during (dashed lines; 5 × 10 Gy), and after IR, compared with untreated tumors in independent mice. Means ± SD (four to seven independent tumors). *, P < 0.01 (difference between irradiated and control tumors at the endpoint [day 13]). Statistics, Mann–Whitney U test. **(G)** Time course of radiation response in representative lesions, compared with nonirradiated control tumors (day 13, images derived from Fig. S1 A). Arrowheads, invasion zone. Asterisks, regression zone. Scale bar, 1 mm. **(H)** MV3 tumoroids invading into a 3D collagen matrix were subjected to a single dose of IR (RTX, 4 Gy) and analyzed 5 d later for both fragmentation of the nucleus and cleaved caspase-3 as transient apoptosis marker. Upper panel, experimental setup and overview image showing tumoroid core (T) and invading cells with closeup of invasion zone. Lower panel, clear distinction of viable and apoptotic cells based on nuclear morphology and cleaved caspase-3 staining. Scale bar, 50 µm.
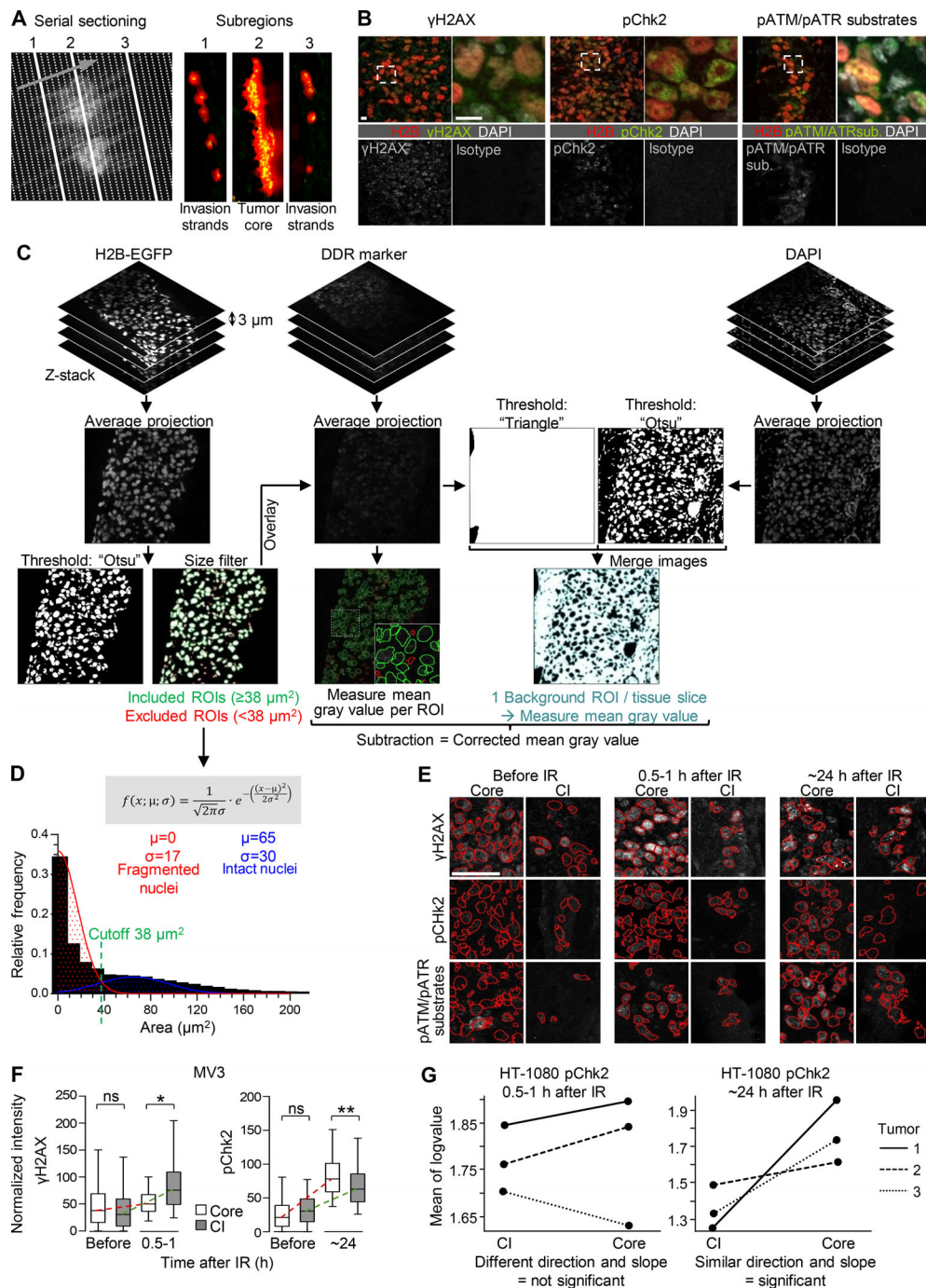
Figure S3. Tumor subregion analysis of the DDR by serial sectioning and image analysis. (A) Principle of serial vertical tumor sectioning and morphology mapping to annotate serial samples from tumor core (region 2) and invasion zone (regions 1 and 3). Arrow, direction of sectioning. **(B)** Specific and isotype-controlled background staining for DDR markers (irradiated samples). Dashed rectangles, region of detail images. Scale bar, 10 μm. **(C)** Workflow for image segmentation and single-cell analysis. ROI, region of interest. **(D)** Histogram analysis of nuclear size distribution to determine the cutoff for exclusion of nuclear fragments (i.e., apoptotic nuclei). Indicated variables and formula were used for Gaussian distribution fitting to define the intersection and separate fragmented from intact nuclei. Area binning of ∼18,000 nuclear ROIs from three independent HT-1080 tumors including cores and invasion zones. Similar distributions and curves were obtained for MV3 tumors resulting in the same cutoff (data not shown). **(E)** Representative γH2AX, pChk2, and pATM/ATR substrate signal in subregions of HT-1080 tumors before, shortly after, or 1 d after single-dose IR. Representative maximum-intensity projections from confocal 3D stacks. Red selections, ROIs of tumor nuclei. CI, collective invasion. Scale bar, 50 μm. **(F)** Quantification of γH2AX and pChk2 signal intensity in MV3 tumors before and after single-dose IR. Data originate from ∼150–600 nuclei per invasion zone and tumor and ∼1,000–6,000 nuclei per core and tumor from two independent tumors, represented as medians, 25th/75th percentiles (box), and 5th/95th percentiles (whiskers). Dashed lines visualize approximate dynamics of DDR. *, P = 0.01; **, P = 0.003; ns, not significant. Statistics, mixed-model ANOVA (see Materials and methods for details). **(G)** Identification of biologically relevant effects from large datasets. Example plots derived from the lmer function after performing a mixed-model ANOVA showing the distribution of mean of log values for different tumor subregions and tumors. Only datasets revealing similar directions and slopes were included for statistical analysis (right plot), whereas samples with disparate or noise-like behaviors (left plot) were considered not significant.
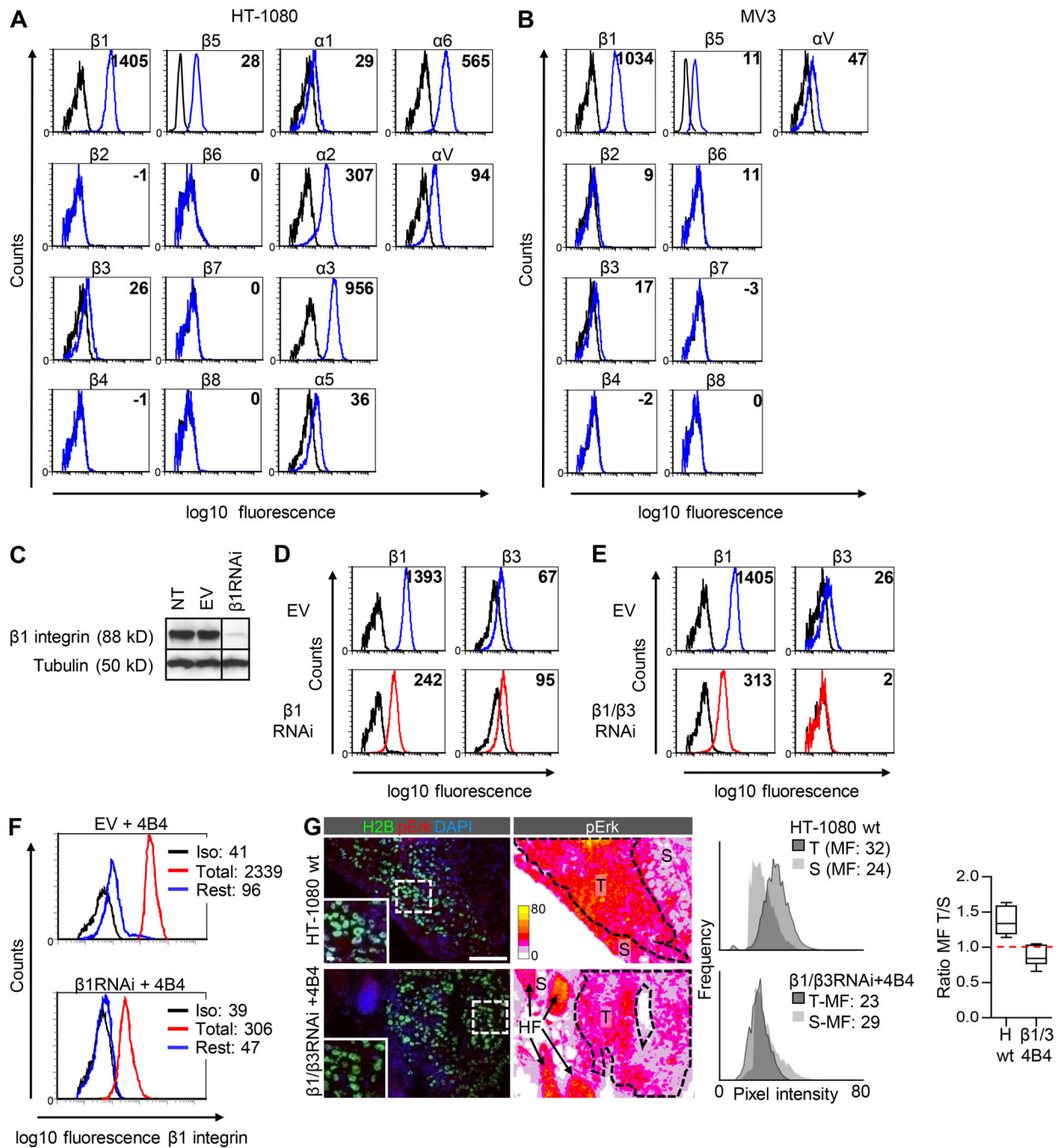
Figure S4. Integrin expression profiles in HT-1080 and MV3 cells and RNAi-based integrin targeting in HT-1080 cells. (A and B) Surface expression pattern of integrin β and α chains on HT-1080 (A) and β chains on MV3 (B) cells determined by flow cytometry. Black line, isotype control. Values, mean fluorescence (minus isotype values). **(C–E)** Downregulation of β1 and β3 integrins in HT-1080 cells by shRNA. **(C)** Knockdown efficiency of β1 integrin in dual-color HT-1080 cells (Western blot), compared with nontransduced (NT) and empty vector (EV)–transduced cells. β-Tubulin, loading control. **(D and E)** Up-regulation of β3 integrins after downregulation of β1 integrin (D) and efficient downregulation of both β1 and β3 integrins after β1/β3RNAi (E) determined by flow cytometry. Surface expression pattern of β1 and β3 integrins on β1RNAi cells or β1/β3RNAi cells (red lines) compared with cells transfected with empty vector (EV, blue lines). Black line, isotype control. Values, mean fluorescence (minus isotype values). Stability of β1/β3 downregulation was routinely verified, and no outlier behavior or drift of expression to other integrin β-chains was noted (data not shown). **(F)** Reduction of β1 integrin adhesion epitope detected by FITC-conjugated mAb 4B4 on vector control (EV; left) and β1RNAi cells (right) after epitope saturation with unconjugated mAb 4B4 (3 µg/ml; blue line showing residual epitopes) compared with unspecific IgG1 (red line; total epitopes). Black line, isotype control staining (Iso). Values indicate mean fluorescence intensities. **(G)** Diminished phosphoErk signal (MAPK signaling) after β1/β3 integrin targeting (day 7). Histograms show the mean pixel fluorescence (MF) intensity of pErk from control (HT-1080 wild type) and β1/β3 integrin targeted tumors (T, dotted lines, identified by H2B-EGFP label) compared with pErk signal in the surrounding stroma (S), which further contained hair follicles (HF) with strong endogenous pErk expression. Ratio of tumor- and stroma-derived pErk intensity is displayed as medians, 25th/75th percentiles (box), and 5th/95th percentiles (whiskers) from one sample determined from 10 independent regions of the corresponding stroma region after exclusion of hair follicles, with a ratio of 1.0 (red dashed line) when signal intensity of both regions was equal. Calibration bar, pixel intensity. Scale bars, 100 µm (overview); 10 µm (inset).

A HT-1080

B MV3

C HT-1080 MV3

○ IgG₁+IgG₁
● IgG₁+IgG₁ IR
◇ 4B4+17E6
◆ 4B4+17E6 IR
-- IR

D HT-1080 MV3

□ Control
■ IR

E HT-1080

H2B Cytoplasm Bloodvessels SHG

F Tumor fluorescence monitoring (Ds-Red2)

Start therapy → Completion therapy Day 20-180 Follow up

G HT-1080

Non-IR 5x4Gy
5x1Gy 5x8Gy
5x2Gy

MV3

30% cure

MV3
HT-1080

H Lymph node Lung

H2B
Ds-Red2

I Exclusion of minimal residual lesions at former tumor spot

H2B Ds-Red2

Screen backside dorsal skin (day 180) (neg.)   Anti-EGFP IHC (neg.)

J H2B-EGFP positive tumor remants

H2B H2B

Backside dorsal skin (former tumor spot) 10 μm tissue cross-section Anti-EGFP IHC
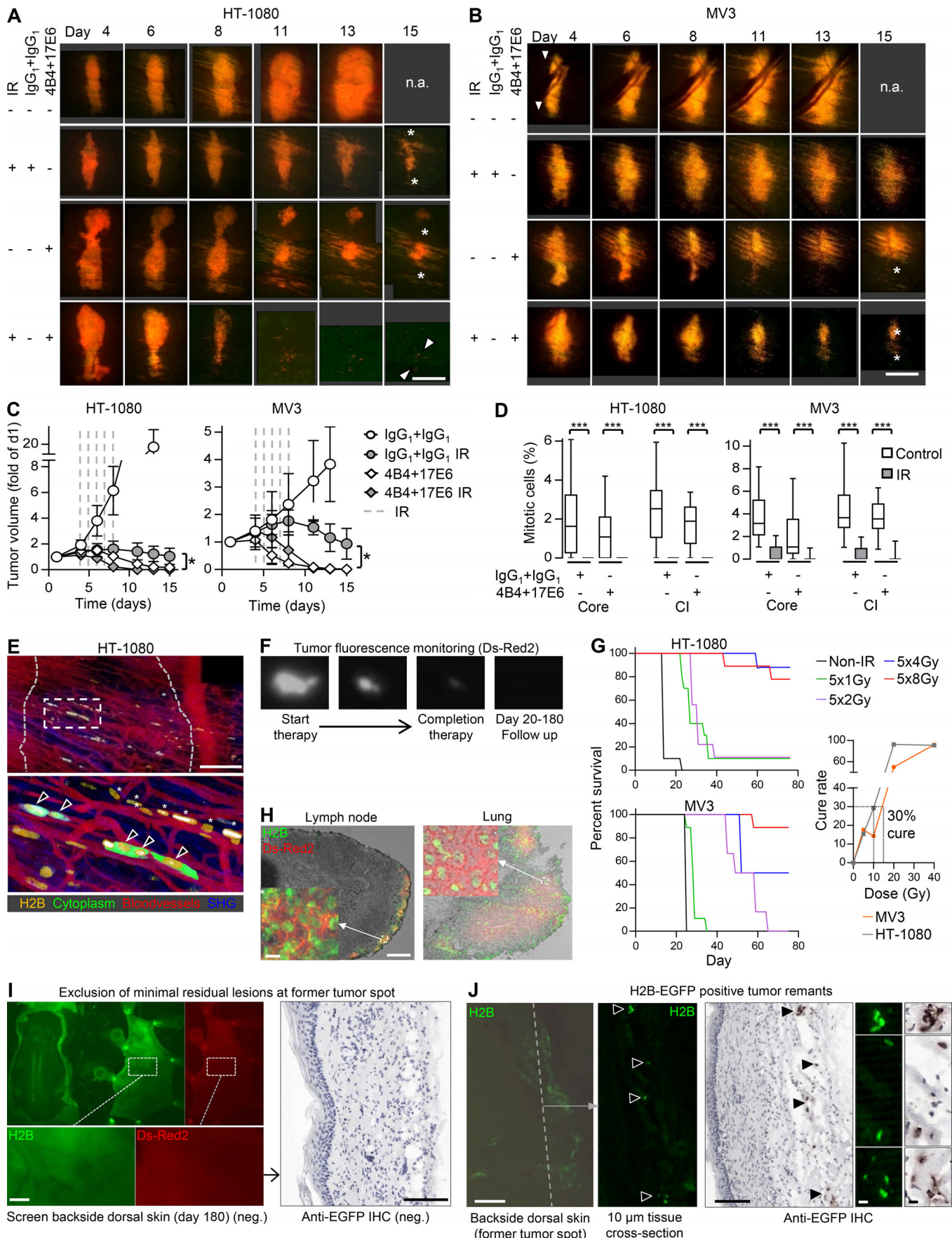
Figure S5. **Radiosensitization of sarcoma and melanoma tumors by antibody-based integrin interference and procedures and outcome of long-term therapy response. (A–D)** Tumor morphology and quantification of radiosensitization assessed by intravital microscopy. **(A and B)** Time-dependent growth or regression of HT-1080 or MV3 lesions in response to the indicated treatment conditions. n.a., not analyzed due to humane endpoint after day 13 (tumor >2 cm³). Images of untreated HT-1080 and MV3 tumors are also shown in Fig. S1 A. Asterisks, regression tumor core. Arrowheads, tumor remnants. Scale bars, 1 mm. **(C)** Time-dependent tumor volume during and after treatment with IgG1 or mAb 4B4 + 17E6 with or without IR. Data show the means ± SD from three to four (HT-1080) or three to five (MV3) independent lesions. *, P = 0.0286 (comparison IgG1/IR control with 4B4/17E6 and IR [day 15]). Statistics, Mann–Whitney U test. **(D)** Mitotic frequencies in nonirradiated and irradiated tumor core and collective invasion (CI) zone. Data show the medians, 25th/75th percentiles (box), and 5th/95th percentiles (whiskers) of 10–20 nuclei per tumor region and condition from 7 to 23 independent fields from four (HT-1080) or three to five (MV3) independent tumors. ***, P < 0.0001. Statistics, Mann–Whitney U test. **(E)** Long-term follow-up (day 26) after treatment with 4B4 and 17E6 and IR, revealing minimal residual disease. Dotted gray line, position of former tumor. Box, position of lower panel. Zoom shows surviving cells without mitotic activity (arrowheads) and cytoplasm-free, condensed nuclei of disintegrated cells (asterisks). Scale bars, 250 μm. **(F)** Example tumor undergoing complete regression after therapy monitored longitudinally by whole-body fluorescence imaging. **(G)** IR dose escalation study for intradermal HT-1080 and MV3 tumors (window-free dermis). Left panels, overall survival after IR using the indicated doses (6–10 mice per group). Right panel, cure rate measured as percentage of tumors that did not relapse after IR. Black dashed line, IR dose with 30% cure rate (5 × 2 Gy for HT-1080 tumors, 5 × 3 Gy for MV3 tumors). **(H)** Dual-color detection of lung and lymph node metastases. Microscopic whole-organ screen (not depicted) was followed by analysis of cryosections (depicted). Scale bars, 100 μm (overview); 10 μm (inset). **(I)** Identification of minimal residual disease at the endpoint. The dorsal skin was screened from the deep fascia for presence or absence of fluorescent tumor remnants (left panel). In case of doubt, subregions were additionally sectioned for analysis by anti-EGFP immunohistochemistry (IHC; right panel). Images show typical tumor-negative outcome. Scale bar, 100 μm. **(J)** Examples of minimal residual lesions present at the tumor implantation site at the endpoint (day 180). Tumor remnants with strand-like pattern of green-fluorescent tumor nuclei (H2B-EGFP) followed by tissue sectioning and validation by anti-EGFP IHC. Dashed line, approximate position of tissue cross section. Arrowheads, intact H2B-EGFP–positive tumor nuclei. Right panel, validation of EGFP-positive tumor remnants and positive anti-EGFP IHC side by side. Scale bars, 100 μm (overview); 10 μm (details).

Table S1. **Survival rates and tumor outcome for long-term follow-up experiments on integrin-targeted and IR therapy in HT-1080 sarcoma xenografts**

Treatment	Negative[a]		Growing primary lesion[b]	Macroscopic tumor relapse[c]	Minimal residual lesion[d]	Metastatic disease[e]
	Frequency	**Percentage**				
IgG1	0/9	0%	9/9	0/9	0/9	0/9
4B4 + 17E6	0/9	0%	9/9	0/9	0/9	3/9
IR + IgG1	3/10	30%	6/10	1/10	0/10	7/10
IR + 17E6	2/9	22%	5/9	1/9	1/9	6/9
IR + 4B4	8/11	72%	1/11	2/11	0/11	3/11
IR + 4B4 + 17E6	8/10	80%	0/10	1/10	0/10	1/10[f]

[a]Lack of growing primary lesion, relapse, minimal residual lesion, or metastasis.
[b]Persisting and increasing fluorescence signal at the tumor implantation site reaching endpoint tumor burden.
[c]Recurring and increasing fluorescence signal at the implantation site after a period of absence of signal (transient regression).
[d]Absence of detectable tumor or fluorescence signal until the endpoint, but presence of H2B-EGFP–positive cells in the dermis.
[e]Presence of fluorescent lesions detected by microscopic screening of lungs and lymph nodes at the humane endpoint after 180 d, unless stated otherwise (compare Fig. 7 D, left panel, for time-dependent end-points for each group).
[f]One mouse with complete regression of primary lesion but distant metastasis.

Table S2. **Survival rates and tumor outcome for long-term follow-up experiments on integrin-targeted and IR therapy in MV3 melanoma xenografts**

Treatment	Negative[a]		Growing primary lesion[b]	Macroscopic tumor relapse[c]	Minimal residual lesion[d]	Metastatic disease[e]
	Frequency	Percentage				
IgG1	0/9	0%	9/9	0/9	0/9	0/9
4B4 + 17E6	0/9	0%	9/9	0/9	0/9	0/9
IR + IgG1	1/12	8%	8/12	1/12	2/12	8/12
IR + 17E6	6/10	60%	3/10	0/10	1/10	2/10
IR + 4B4	3/8	38%	1/8	1/8	2/8	3/8[f]
IR + 4B4 + 17E6	10/11	91%	0/11	0/11	1/11	0/11

[a]Lack of growing primary lesion, relapse, minimal residual lesion, or metastasis.
[b]Persisting and increasing fluorescence signal at the tumor implantation site reaching endpoint tumor burden.
[c]Recurring and increasing fluorescence signal at the implantation site after a period of absence of signal (transient regression).
[d]Absence of detectable tumor or fluorescence signal until the endpoint, but presence of H2B-EGFP–positive cells in the dermis.
[e]Presence of fluorescent lesions detected by microscopic screening of lungs and lymph nodes at the humane endpoint after 180 d, unless stated otherwise (compare Fig. 7 D, right panel, for time-dependent end-points for each group).
[f]One mouse with complete regression of primary lesion but distant metastasis.
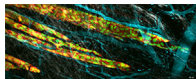
Video 1. **Collective invasion strands of a HT-1080 sarcoma xenograft.** Time-lapse microscopy of a maximum projection. Duration, 3.5 h. Field size 815 × 323 µm. Frame rate, every 7 min, with 7 frames/s playback. The video corresponds to Fig. 1 B.
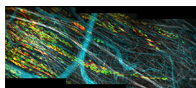
Video 2. **Collective invasion strands of a MV3 melanoma xenograft.** Time-lapse microscopy of a maximum projection. Duration, 4 h. Field size 1,100 × 477 µm. Frame rate, every 7 min, with 7 frames/s playback. The video corresponds to Fig. 1 B.
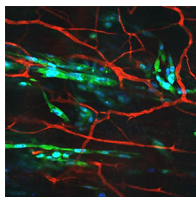
Video 3. **Differential radiation response in tumor core and collective invasion niche in HT-1080 sarcoma xenografts detected by intravital microscopy.** High-resolution reconstructions of radiosensitive and radioresistant regions. 3D image stacks of nonirradiated control tumors and tumors after hypofractionated IR (5 × 8 Gy) on day 14 after implantation. Channels: blue, H2B (nuclei tumor cells); green, DsRed2 (cytoplasm tumor cells); red, Alexa Fluor 660–dextran (perfused blood vessels, phagocytes). Image volume, 500 × 500 × 250 µm (control) and 500 × 500 × 120 µm (irradiated).